remote sensing

MDPI

Article

Spectral Unmixing of Coastal Dune Plant Species from Very High Resolution Satellite Imagery

Katerina Kombiadou [1,*], Susana Costas [1], Juan Bautista Gallego-Fernández [2], Zhicheng Yang [3], Luisa Bon de Sousa [1] and Sonia Silvestri [4]

[1] Center for Marine and Environmental Research (CIMA)/ARNET, University of Algarve, Campus of Gambelas, 8005-139 Faro, Portugal; scotero@ualg.pt (S.C.); mlssousa@ualg.pt (L.B.d.S.)
[2] Departamento de Biología Vegetal y Ecología, Universidad de Sevilla, 41012 Sevilla, Spain; galfer@us.es
[3] Department of Marine Sciences, University of Georgia, Athens, GA 30602, USA; zhicheng.yang@uga.edu
[4] Department of Biological, Geological, and Environmental Sciences, University of Bologna, P.za Porta S. Donato 1, 40126 Bologna, Italy; sonia.silvestri5@unibo.it
* Correspondence: akompiadou@ualg.pt

Highlights

What are the main findings?

- Spectral unmixing with random forest regressor showed good skill in terms of detecting the fractional cover of major dune plant species but performed poorly for small-stemmed or less abundant species.
- Model accuracy was enhanced when including the distance to the shoreline in the predictor dataset, with a significantly lower influence when including surface elevation data.

What are the implications of the main findings?

- Class abundance and plant characteristics (spectral signature and fractional cover within the pixel) are significant limiting factors for the detectability of a class.
- Enhancing broadness and resolution of spectral data used with unmixing algorithms may be the key to improving the segregation of plants or plant groups in highly mixed coastal dunes.

Abstract

While improvements in the spectral and spatial resolution of satellite imagery have opened up new prospects for large-scale environmental monitoring, this potential has remained largely unrealised in dune ecogeomorphology. This is especially true for Mediterranean coastal dunes, where the highly mixed and sparse vegetation requires high resolution satellites and spectral unmixing techniques. To achieve this aim, we employed random forest regressors to predict the fractional cover of dune plant species in two of the sandy barriers of Ria Formosa (S. Portugal) from WorldView-2 imagery (June 2024). The algorithm, tested with spatially upscaled multispectral drone data and satellite imagery, detected the fractional cover of major species (most abundant classes and bushy vegetation) with reasonable to very good accuracy (coefficient of determination, CoD: 0.4 to 0.8) for the former and reasonable to good accuracy (CoD: 0.4 to 0.6) for the latter. Additional tests showed that (a) including the distance to the shoreline can increase model accuracy (CoD by ~0.1); (b) the grouping of species resulted in an insignificant increase in model skill; and (c) testing over independent dune plots showed generalisation beyond the training set and low risk of overfitting or noise. Overall, the approach showed promising results for large-scale observations in highly mixed coastal dunes.

check for updates

Academic Editor: Kevin Tansey

Received: 5 November 2025
Revised: 4 December 2025
Accepted: 6 December 2025
Published: 10 December 2025

Citation: Kombiadou, K.; Costas, S.; Gallego-Fernández, J.B.; Yang, Z.; Bon de Sousa, L.; Silvestri, S. Spectral Unmixing of Coastal Dune Plant Species from Very High Resolution Satellite Imagery. *Remote Sens.* **2025**, *17*, 3991. https://doi.org/10.3390/rs17243991

Keywords: dune species; subpixel remote sensing; WorldView-2; multispectral data; fractional cover; random forest regressor

1. Introduction

Identifying changes in plant communities is a conservation priority, especially for Mediterranean coastal dunes that harbour some of the most threatened habitats in Europe [1]. Ecogeomorphic links, fundamental to the self-organisation capacity of coastal dunes [2], suggest that a shift in plant community structure and composition (i.e., expansion of invasive species) can produce an important change in the structure and function of coastal dune ecosystems [3], which, in turn, can induce changes to the topography itself [4,5]. Such changes and domino effects can potentially cripple previously established adaptation mechanisms and lead to a (permanent or temporary) system tipping point [6]. These considerations advocate for systematic, large-scale, monitoring of coastal dune vegetation, especially in protected areas and in fragmented and stressed dune environments (e.g., due to nutrient fluxes and/or precipitation rates, human impacts, squeezed conditions, etc.) [7]. Such efforts should focus not only on habitat conservation status, but on potential implications for the contemporary and near-future resilience of these sensitive sentinels of climate change [8]. While traditional field surveying is the most widely used method of vegetation mapping, it is time-consuming, expensive, and limited in spatial coverage [9]. Remote sensing, on the other hand, provides alternative means to obtain large-scale and standardised vegetation identification data [10].

Remote sensing applications typically use hyper- or multi-spectral data obtained by Unmanned Aerial Vehicles (UAVs) and employ vegetation indices (e.g., [11]), supervised (e.g., Maximum Likelihood, support vector machine (SVM), random forest (RF), and Artificial Neural Network (NN)) and unsupervised (e.g., K-means) classification techniques to map dune vegetation cover [11], habitats [12], plant taxa [13], or individual plant species [14]. Overall, pixel-based classification is more common in highly mixed coastal dunes; however, depending on the required resolution of the analysis, object-based classifications may perform better, reducing 'salt and pepper' effects [15]. Belcore et al. applied an object-based image analysis algorithm on multispectral UAV data from coastal dunes in Tuscany (Italy), detecting and classifying 12 different plant species, as well as sand and debris, with an average accuracy of 75% for training and 62% for unseen data [16,17]. Aside from classification, machine learning techniques like RFs and SVMs can be employed in regression tasks to estimate continuous vegetation parameters. RF regression, for example, achieved the highest overall accuracy (0.89) among five supervised classification algorithms for the detection of the fractional cover and aboveground biomass of *Caprobrotus edulis* from UAV multispectral images from the sand dunes of the Cávado River spit (north of Portugal) [18]. Deep learning techniques have also been employed in large-scale monitoring approaches, like the Convolutional NN trained to map coastal dune habitats (four vegetated classes: shrubs, grasses, broadleaf, and needleleaf trees) throughout the Dutch coast with high accuracies (an overall accuracy of 0.92) even using only RGB UAV data at a 25 cm resolution [19].

Even though improvements in spatial, spectral, and temporal resolution in satellite imagery and advances in remote sensing techniques have increased capabilities for regular and large-scale coastal monitoring and observation [20], this potential has not been fully capitalised for coastal dune habitats. This is mainly due to the small size and density of plants and the complexity and heterogeneity of the existing species that inhibit coastal dune vegetation species identification [7]. Indeed, vegetation characterisation can be

challenging in the presence of short and sparse canopies or of highly mixed populations, as is usually the case in Mediterranean coastal dune systems [21]. Similarly to works using UAV data, satellite remote sensing applications either focus on mapping the boundaries of the dune environment using vegetation indices (e.g., [22]) or on classifying individual species (e.g., [7]). Kozhoridze et al., for example, used coarse Landsat time series data to reconstruct the past dynamics of plant expansion of two focal invasive species (*Heterotheca subaxillaris* and *Acacia saligna*) in the Mediterranean coastal plain of Israel [23]. Marzialetti et al. identified and mapped five vegetation classes organised into three hierarchical levels, applying a phenology-based RF classification on Sentinel-2 (S2) images on a Mediterranean coastal dune [24]. A later work [25] used similar approaches (hierarchical clustering and a RF model) and S2 imagery to produce an unsupervised land cover map, distinguishing four dune types in a representative site of the Adriatic coast. Limited in their analysis by the pixel size of the S2 product, the same authors advocated for using higher spatial resolutions and/or subpixel classification methodologies to improve results [24,25]. Gupta et al. tested varying resolutions of multispectral imagery from UAVs and satellites (Vision-1, PlanetScope (PS), and S2) and RF classification to map the expansion of an invasive species (*Heterotheca subaxillaris*) in the coastal dunes of the eastern Mediterranean, with results supporting the critical role of spatial resolution for plant identification in highly mixed coastal dune environments [26]. Similarly, RF models calibrated to identify the expansion of *Acacia saligna* in the Adriatic coast of central Italy, were able to delineate invaded area edges and small patches more effectively in PS than in S2 [27]. Medina Machín et al. applied an SVM classifier to discriminate between six coastal dune species (Gran Canaria, Spain) at the pixel level using WV2 imagery, with the approach showing acceptable capability for dune shrubs [7]. The results of these works indicate that hard classification approaches (i.e., assigning one 'dominant' class to each individual pixel) are very limiting in highly mixed environments (i.e., those containing many plants with small plant parts and low fractional cover), even considering very high resolution satellite products [24,28]. Such environments require unmixing approaches that capture the fine-scale spatial distribution of vegetation species within each pixel [29].

Spectral unmixing, a group of techniques that attempt to decompose the spectral signal of mixed pixels into contributions of individual endmembers and associate them to endmember fractional abundance within the pixel [30], has been used for mapping a wide range of landcover types over a wide range of spatial and spectral resolutions (UAV to satellite and multi- to hyper-spectral data). Especially regarding highly mixed coastal habitats, unmixing RF models, like soft classification [28] and rescaled regression [29], have shown promising results in predicting the fractional cover of the main plant species in salt marshes from satellite imagery at a subpixel level. To date and to our knowledge, only the works of Ettritch et al. [31], Medina Machín et al. [7], and Pafumi et al. [32] have employed spectral unmixing techniques for coastal dune observation from satellite imagery. Ettritch et al. applied a linear unmixing model to Landsat 8, WV2, and UAV imagery from Kenfig Burrows (UK) to estimate bare sand (or total vegetation) cover, as a proxy for ecological dune stabilisation [31]. Pafumi et al. tested hard and soft RF classification approaches to map coastal dune habitats (Tuscany, Italy) on WV3 imagery, observing that while soft approaches captured a more realistic representation of vegetation patterns, hard RF classification produced more accurate results for coastal dune scrubs and white dunes [32]. Medina Machín et al. tested linear unmixing techniques using spectral signatures from field radiometric measurements on WV2 imagery; however the approach performed worse than the application of a hard SVM classifier, trained with corrected WV2 multispectral bands plus a vegetation index (MSAVI2) and a band of contextual information (variance of the first principal component) [7]. In these works,

spectral unmixing was employed to discriminate classes with cover that typically exceeded the size of the WV2 pixel (e.g., shrubs). The applicability of such methods in more highly mixed coastal dunes remains unexplored.

The present work aims to assess the potential of spectral unmixing techniques (namely RF regressors) to discriminate plant species and predict their fractional cover in the sparsely vegetated coastal dunes of south Portugal. To do so, we employ RF regressors and very high resolution satellite imagery from WV2, combined with multispectral UAV data, used both as ground truth and as training and testing data. The analysis focuses on analysing the approach, identifying strengths and limitations, and proposing directions for further research.

2. Materials and Methods

The main objective of the analysis is to assess the usability of machine learning algorithms, like RF, and imagery from very high resolution satellite sensors, like WV, to identify dune plants in Mediterranean coastal dunes, like the Ria Formosa barrier system. To do so, we used the following:

- Ground truth data for dune plant distribution and cover, obtained from UAVs, as targets.
- Multispectral data from three remote sensing platforms (in order of decreasing spatial resolution: UAV, WV2, and PS), as predictors.
- Regression models (RF, SVM, and histogram gradient boosting; HGB), as estimators.

The main UAV and WV2 regression tests were performed over the same spatial grid (i.e., WV2 pixels), to allow for comparability of model skill. Complementary analyses (spectral signatures and hard RF classification) were also performed to assess the spectral similarities between plant species, using high-resolution UAV multispectral data. Details on the study site, the spectral and ground truth data collected, and the approach and data processing steps are given in the following subsections.

2.1. Study Site

The work focuses on the dunes along the barrier island chain of Ria Formosa in South Portugal (Figure 1). Ria Formosa is a natural park (since 1987), it is protected under the Ramsar convention, and is part of the EU Natura 2000 network. The sandy barriers of the system host three dune habitat types included in the Annex I of the European Habitat Directive 92/43/EEC: 2110 'Embryonic shifting dunes', 2120 'Shifting dunes along the shoreline with *Ammophila arenaria*' (white dunes), and 2130 'Fixed coastal dunes with herbaceous vegetation' (grey dunes) [33], among which types 2110 and 2130 are characterised as priority habitats.

The climate in the region is classified as Csa following the Köppen–Geiger classification system [34], characterised as temperate with dry or hot summer. The monthly average temperature ranges between 12.3 and 24.6 °C and the total annual rainfall is about 450 mm/y (1991–2020 climatic mean data from [35]). These conditions are linked to relatively low dune vegetation cover over, ranging from 10 to 50% over the stoss slope and from 50 to 90% over the dune crest [33].

Figure 1. WV2 imagery obtained in June 2024 over the AOI of Ria Formosa (S. Portugal; location in inset map). The location of plots where ground truth data (UAV flights and plant identification) were collected at the barriers of Ancão and Tavira are shown as stars, along with the orthomosaics obtained in the 4 plots (AncW, AncE, TavW, and TavE).

2.2. Datasets

2.2.1. WV2 Imagery

The WV2 imagery (Ortho-Ready Standard 2A radiometrically balanced surface reflectance values over 8 multispectral bands at 2 m and 1 panchromatic band at 0.5 m; cloud cover of 0% and off-nadir angles below 12° at image capture) was obtained over the barrier island chain of Ria Formosa (Figure 1) on 21 June 2024. Image acquisition was over an Area of Interest (AOI) of around 250 km^2 and barrier length of around 54 km. The 8 multispectral bands were pansharpened using the panchromatic band and the Gram–Schmidt method with nearest neighbour resampling [36] through the ENVI (v5.6) software [37].

2.2.2. UAV Data

Ground truth data were collected in the barriers of Ancão and Tavira (Figure 1) using two UAVs, the Phantom 4 Multispectral (DJI, Shenzhen, China; hereafter P4M), collecting images with a camera array of 5 sensors (blue (B; 450 nm), green (G; 560 nm), red (R; 650 nm), red edge (RE; 730 nm), and near-infrared (NIR; 840 nm)); and the Mavic 2 Pro (DJI; hereafter M2P) capturing high-resolution RGB imagery. Two dune plots were surveyed at each barrier (Figure 1; Table 1), covering the dune habitats from the embryonic dune to the back dune. The flights adhered to the recommendations of Bon de Sousa et al. for minimising associated errors by employing low-flying and intermediate (30–40°) sun altitudes and overlapping perpendicular flights with a minimum of 6 ground control points (GCPs) per plot hectare, regularly dispersed in a diamond grid [38]. All flights were performed within 2 weeks of WV2 acquisition (8 to 12 of July), meaning that dune vegetation did not change between satellite and UAV captures. The position of GCPs and

independent check points was recorded using an RTK-DGPS and the Agisoft Metashape (v1.7.2) software was used to georeference images and obtain orthophoto mosaics and a digital surface model (DSM) of the plots using structure from motion. Information on the UAV flights and the accuracy metrics of the products are given in Table 1.

Table 1. Information on processed data collected with Phantom 4 Multispectral (P4M) and Mavic 2 Pro (M2P) over the 4 dune plots (RMSE: root mean square error; GCP: ground control points; DSM: digital surface model).

Parameter	UAV	Dune Plot			
		AncE	AncW	TavE	TavW
Flight date (2024)	both	8 July	9 July	11 July	12 July
Plot area (cross-shore × alongshore dimension, in m)	both	100 × 140	140 × 120	75 × 180	85 × 135
Flying altitude (m)	P4M	35.6	32.7	28.6	29.7
	M2P	31.5	31.5	32.1	29.8
Number of GCPs	both	13	15	13	16
Ground resolution (cm/pixel)	P4M	1.63	1.57	1.4	1.46
	M2P	0.68	0.68	0.68	0.65
RMS reprojection error (pixel)	P4M	0.425	0.366	1.12	0.373
	M2P	0.647	0.475	0.71	0.65
GCP RMSE (mm)	P4M	13.61	21.73	6.05	7.57
	M2P	30.11	21.07	14.35	19.35
DSM RMSE (mm)	M2P	7.12	11.31	6.84	8.45

Plots AncE and TavW were used to train and test the algorithm, while plots AncW and TavE were used to test the trained model against unseen data. P4M imagery was used to (a) sample the spectral signatures of dune plant species and analyse spectral similarity between them to assess the need for grouping species during regression, (b) obtain ground truth data for the fractional cover (FC) of plant species, and (c) to train the algorithm using upscaled raster datasets of the 5 bands at the WV2 grid (obtained using the Zonal Statistic Mean from ArcGIS). Aside from DSMs, M2P orthophotos were used for visual identification and mapping of plants in each plot, due to their higher spatial resolution than P4M (Table 1).

2.3. Remote Sensing Approach

As the variability of species and plant morphometric characteristics in the domain is very high, the application of hard classification (i.e., assigning a class to each individual pixel) approaches is (a) not meaningful at the WV2 pixel scale (i.e., sensing one 'dominant' class over 0.5 m × 0.5 m) and (b) not feasible at the P4M pixel scale. To capture the presence of fine-stemmed or small-leafed plants, the spatial resolution would need to be maintained at a very high level. For example, an average leaf of *Calystegia soldanella* covers an area around 35–40 cm^2, while the width of *Otanthus maritimus* stems is around 2–4 cm and *Ammophila arenaria* stems measure below 1 cm, corresponding to 13–16, 1–2, and less than 1 pixels of the P4M imagery in AncE. It follows that individual pixels may still be mixed, even at the original P4M resolution (1.4–1.6 cm; Table 1), while pixel-by-pixel classification would be extremely resource intensive. We, therefore, mainly focus on the applicability and accuracy of subpixel (i.e., spectral unmixing) algorithms for the identification of dune plants, only employing hard classifiers to identify spectral separability of plants.

The RF regressor (hereafter RFR) is an ensemble-based learning algorithm that improves predictive accuracy, stability, and generalisation through the aggregation of multiple regression trees to obtain predictions [39]. Each tree is trained on a bootstrap sample of the original dataset, introducing randomness in both sample selection and feature choice

during node splitting [39]. By reducing correlation among individual trees, the randomness significantly lowers model variance, without notably increasing bias [40]. We applied the RFR using the SciKit [41] and trained separate forests to predict the FC of each class (target; dependent variable) with spectral data (features; independent variables) from P4M and WV2. The predicted FC values from the individual RFRs were proportionally readjusted so that the sum of all classes equals 1, following the approach of Yang et al. [28,29].

To obtain the features and target datasets necessary to train and test the algorithm at the resolution of the WV pixel grid, ground truth data were processed through a series of steps (see Figure 2). The first step was to obtain ground truth values of the vegetation distribution in the field, which was expressed by the Fractional Vegetation Cover (i.e., the FC of total vegetation in the field; hereafter referred to as FC_{veg}), which is an essential phenotypic factor that makes it possible to characterise the spatial pattern of vegetation types [42]. FC_{veg} is defined as the vertical projection areal proportion of the landscape occupied by green vegetation and has been found to vary linearly with NDVI in coastal dune environments [43,44], semi-arid landscapes [45], and desert environments [46]. Based on this, FC_{veg} was calculated through the linear model [47]

$$FC_{veg} = \frac{NDVI - NDVI_S}{NDVI_V - NDVI_S} \quad (1)$$

where NDVI is the Normalised Difference Vegetation Index of the pixel and $NDVI_S$ and $NDVI_V$ are the values of fully bare (FC_{veg} = 0) and fully vegetated (FC_{veg} = 1) pixels, respectively. These threshold values were determined from the distribution of NDVI in the plots of AncE and TavW at the original P4M pixel size. For $NDVI_S$, tests were performed in both plots to find a cutoff value that adequately separating sand from vegetation, finding the most accurate separation for $NDVI_S$ = 0.05. $NDVI_V$ was set to 0.75, value determined by the topmost cluster of NDVI, obtained by applying the natural breaks (Jenks) method [48] with 20 classes.

As imagery resolution has a significant impact on remote sensing of vegetation cover in dunes, the highest resolution imagery available should be employed for its determination [49]. Therefore, Equation (1) was applied at the original resolution of the P4M flight, to obtain a raster with the values of FC_{veg} over the dune plots. The FC_{veg} raster was then separated into individual dune plant species using plant boundary polygons, mapped on the high-resolution M2P orthophotos to allow for more accurate visual identification of plant species. Considering the characteristics of the vegetation (the high mixing of species and the small size of plants and plant parts), manual separation of plant species was deemed as the most viable and dependable option to minimise any error and uncertainties introduced to the reference dataset. These plant boundaries were drawn so that non-green areas that may reflect high in the NIR range and thus show high NDVI values, such as dead vegetation (dried branches and plant parts) and shadows, were excluded from the FC of the dune plant species ($FC_{veg(i)}$). The excluded zones were assigned to class 'DeadV', while the areas with $NDVI \leq NDVI_S$ were assigned to class 'SandB' as follows:

$$\begin{cases} FC_{DeadV} = FC_{veg} - \sum_{i=1}^{ns} FC_{veg(i)} \\ FC_{SandB} = 1 - FC_{veg} \end{cases} \quad (2)$$

$$\Rightarrow \sum_{i=1}^{ns} FC_{veg(i)} + FC_{SandB} + FC_{DeadV} = 1 \Rightarrow \sum_{i=1}^{im} FC_i = 1$$

where ns is the total number of species present in each plot. Of course, the sum of the FC of all classes (im = ns + 2) equals 1.

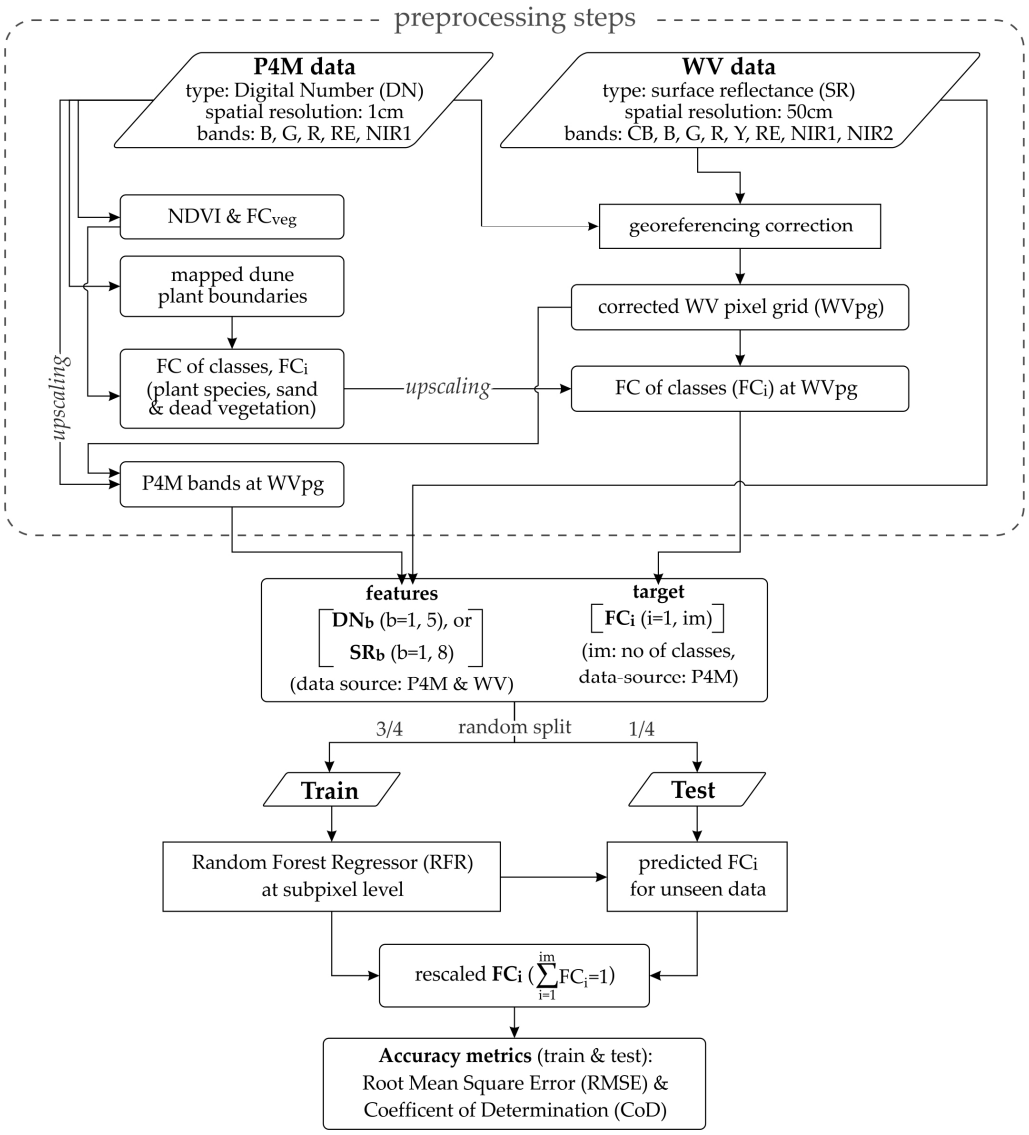

Figure 2. Data preprocessing steps to obtain the observation dataset (features: spectral data from WV or P4M and target FC values for each class from P4M), used to train and test the random forest regressor (RFR) spectral unmixing algorithm. RFR is trained separately for each class and the predicted FC values are then rescaled so that the total for each pixel equals 1.

After obtaining raster datasets of the FC of each class (FC_i) at the resolution of P4M, these were upscaled to the WV2 resolution (Figure 2), using the mean function of the zonal statistics tool in ArcGIS. This method was preferred to other upscaling tools (e.g., the resample tool), as it makes it possible to specify the desired pixel grid. The same tool was used to upscale the 5 multispectral P4M bands to the resolution of the WV2 image. An example of the process, from the segregation of individual $FC_{veg(i)}$ to upscaling, is given in Figure A1 (for the *Artemisia crithmifolia* species in TavW). Data (upscaled class FCs, P4M bands, and WV2 surface reflectance values) were extracted and used for training and testing the algorithm.

After the application of the model, each of the individually trained (one for each class) RFR forests produces the predicted FC values of each class (FC_i). As mentioned, predicted FC values were rescaled to sum to 1, readjusting the excess (or missing) total FC in each pixel proportionally between the classes (Figure 2). After rescaling, the predictive skill of

the model was assessed using the coefficient of determination (CoD) and the root mean square error (RMSE) as goodness-of-fit indicators. The CoD ranges between $-\infty$ and +1 and expresses the ratio of the variability of observations (O_i) effectively captured by the predictions (P_i), while RMSE gives a measure of the average error in the predicted FC for each class as follows:

$$CoD = 1 - \sum_{i=1}^{m}(O_i - P_i)^2 \Big/ \sum_{i=1}^{m}(O_i - \overline{O})^2 \quad (3)$$

$$RMSE = \sqrt{\sum_{i=1}^{m}(O_i - P_i)^2/m} \quad (4)$$

where $\overline{O}$ is the average observation of the class.

The main RFR model hyperparameters were tuned through sensitivity tests (see Appendix A.1), aimed at optimising model skill, while taking care to avoid overfitting. Based on the sensitivity results, the main tuning parameters [50] were set at NTree = 500 and max_depth = 15, while min_samples_split was maintained at the default value of 1/4.

The spectral similarity of classes in each plot was assessed through the high-resolution P4M multispectral data. Pixel values were extracted for the main plant species in the field, for non-vegetated areas (class SandB) and for areas of shadows and dead plant parts (class DeadV). A minimum of around 100 pixels per class per dune plot was maintained, whereas points were spatially distributed as much as possible, to capture the spectral variability of the classes within the domains and the high-resolution multispectral dataset. These values were analysed calculating percentiles of the distribution of spectral data in each class and the Spectral Angle (SA), which was used as an indicator of spectral similarity between classes [51] as follows:

$$SA = \cos^{-1}\left(\sum_{b=1}^{bm} x_b \cdot y_b \Big/ \sqrt{\sum_{b=1}^{bm} x_b^2 \cdot \sum_{b=1}^{bm} y_b^2}\right) \quad (5)$$

where x_b and y_b are the two spectra to compare and bm is the total number of available bands. The SA ranges between 0 and pi/2 radians for identical and as-different-as-possible spectra, respectively. Additionally, the extracted multispectral data were used to test hard RF classifications in the dune plots, interpreting the accuracy of each class as another indicator of the spectral separability.

3. Results

As mentioned, the dune plots AncE and TavW were used for training and testing the subpixel RFR model and the remaining two plots (AncW and TavE) were used for independent testing of the trained model. Therefore, aside from the out-of-sample testing of the trained RFR, the results presented in this section refer to the dune plots AncE and TavW, and include the following:

- The distribution and FC of plant species in the field (Section 3.1).
- The assessment of species separability from native resolution P4M data, based on spectral statistics, SA values, and hard RF classification results (Section 3.2).
- The accuracy of spectral unmixing RFR with M4P data, resampled at the WV2 pixel size, for unseen data. The potential of improving model results by integrating morphological data (distance to shore and elevation) and by grouping species based on their spectral similarities are also investigated (Section 3.3.1).

- The accuracy of spectral unmixing of RFR with WV2 data, for unseen data, as well as a comparison with RFR using PS data; gains in model skill by integrating morphologic data (distance to shore and elevation) are also analysed for the WV2 application (Section 3.3.2).

Part of these analyses (e.g., application of RFR with PS), along with additional evaluations (e.g., model sensitivity to hyperparameters) are provided in Appendix A and not as part of the main manuscript for brevity and consistency.

3.1. Plant Species Fractional Cover

The variability of the main plant species in AncE and TavW is given in Table 2 as percent of WV pixels where each class was identified (e.g., a value of 100% means a class is present in all pixels; not to be confused with the class FC), and as FC values in the boxplots of Figure 3. In both cases, values are shown for the entire plot and only over the foredune ridge. The boxplots in Figure 3 only considered FC values that exceeded 0 (i.e., pixels where the plant was present), to avoid skewing the distribution toward low values.

Table 2. Class presence and number of pixels used for training and testing in AncE and TavW, with reference to the entire plot and only the foredune ridge. Class presence is given as percentage of WV2 pixels where the class was registered (e.g., 100% presence of SandB means that the class is present in all pixels, meaning that no pixel is fully vegetated): lines 1 to 16 correspond to mapped plant species (the full name and the abbreviation used herein are given; abbreviations are a combination of the first four letters of the genus name and the initial letter of the species name), while lines 17 and 18 correspond to classes 'DeadV' and 'SandB', respectively.

a/a	Classes Name	Abbreviation	Presence in AncE Plot (in %) Entire Plot	Foredune Ridge	Presence in TavW Plot (in %) Entire Plot	Foredune Ridge
1	*Ammophila arenaria*	AmmoA	0.47	0.92	3.61	7.38
2	*Anthemis maritima*	AnthM	0.00	0.00	55.54	19.28
3	*Artemisia crithmifolia*	ArteC	27.11	12.89	5.07	10.12
4	*Calystegia soldanella*	CalyS	4.24	8.28	0.00	0.00
5	*Carpobrotus edulis*	CarpE	0.00	0.00	4.21	1.05
6	*Cladonia foliacea*	CladF	0.00	0.00	18.01	0.00
7	*Crucianella maritima*	CrucM	2.41	4.27	1.21	3.05
8	*Eryngium maritimum*	ErynM	5.69	11.10	0.05	0.00
9	*Helichrysum italicum*	HeliI	0.18	0.00	66.26	22.46
10	*Medicago marina*	MediM	3.97	7.10	0.00	0.00
11	*Otanthus maritimus*	OtanM	0.50	0.87	0.36	0.93
12	*Pancratium maritimum*	PancM	1.61	2.16	0.00	0.00
13	*Paronychia argentea*	ParoA	30.02	0.00	0.00	0.00
14	*Seseli tortuosum*	SeseT	0.00	0.00	0.03	0.00
15	*Silene nicaeensis*	SileN	28.32	0.88	0.00	0.00
16	*Thymus carnosus*	ThymC	0.00	0.00	7.63	4.86
17	Dead vegetation/shadows	DeadV	94.35	92.97	79.58	53.01
18	Sand bare	SandB	100.00	100.00	100.00	100.00

Number of Pixels in Training/Testing	AncE Plot Entire Plot	AncE Plot Foredune Ridge	TavW Plot Entire Plot	TavW Plot Foredune Ridge
training population	38,619	19,775	35,637	14,019
testing population	12,873	6592	11,879	4673

The data show that ParoA, SileN, and ArteC are the plant species with the highest expansion in AncE (Table 2). The former two show low FCs (median values of 1.8% and 0.74%; Figure 3a) and appear almost exclusively over the back dune (i.e., low to no presence in the foredune). ArteC is present throughout the dune plot and, being a shrub, is also the

plant species with the highest FC (median of 21.6% in the domain to 24.3% in the foredune). Classes ErynM, CalyS, and MediM are also highly present in the zone of the foredune ridge, with median FC values of 3.7%, 2%, and 2.2% (Figure 3a). The remaining plant classes in decreasing order of expansion are HeliI, CrucM, OtanM, AmmoA, and PancM (median FCs: 11%, 4%, 3.7%, 3.5%, and 1.5%; Figure 3a).

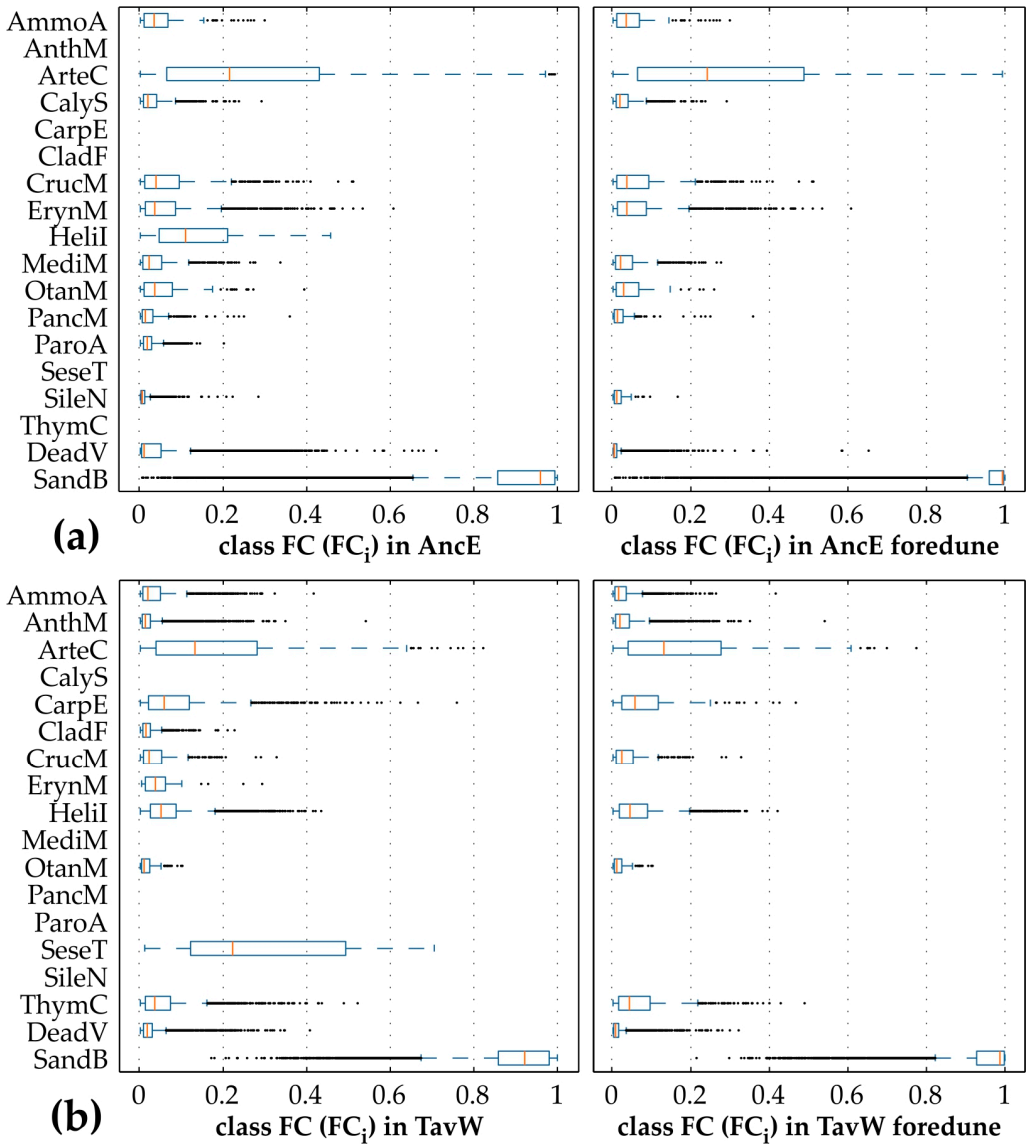

Figure 3. Boxplots of FC of classes of AncE (**a**) and TavW (**b**), with reference to the entire plot (**right**) and only the foredune (**left**); the values were calculated using only the WV pixels where each plant species was present (see Table 2 for values, as well as plant species abbreviation explanation).

For TavW, HeliI has the highest overall presence, especially within the back dunes, and relatively high FCs (median of 4.5–5.2%; Figure 3b), with AnthM, CladF, and ThymC also being widespread (Table 2). AnthM and ThymC show slightly higher FCs along the foredune ridge (2% versus 1.4% for AnthM and 4.4% versus 3.6% for ThymC; Figure 3b), mainly due to the higher NDVIs of plants compared to the back dune (lower FC of DeadV). ArteC, though significantly less dominant than in AncE, is mostly abundant in the foredune of TavW (median FC of around 13%). CarpE is a non-native, invasive species with a relatively high presence, especially in the back dune, and a median FC of around 5.8%. The remaining species of CrucM, OtanM, ErynM, and SeseT have low occupancy in the field.

3.2. Spectral Signature of Plant Species

3.2.1. Plant Spectra

The individual spectra of dune vegetation and bare sand, composing 5 bands from the P4M (shown as 25th, 50th, and 75th percentiles and individual band boxplots in Figure A2 for AncE and in Figure A3 for TavW), indicate that CladF, ErynM, HeliI, DeadV, and SandB appear spectrally distinct and therefore the classes should, in principle, be separable by the algorithm. Conversely, there is significant overlap in the signatures of: (a) AnthM with ThymC, (b) CrucM with AmmoA, and (c) CarpE with ArteC, indicating that these species likely cannot be distinguished. Partial overlap is also noted over the R, G, and B bands between ParoA and OtanM, and in the R, RE, and NIR bands between (a) CalyS and CarpE, and (b) ArteC, MediM, and CrucM.

To quantify how similar (or different) the individual class spectra are, we calculated the SA (Equation (3); Figure 4), whereby low SA values express high similarity and vice versa. A typical threshold value for SA, used to separate spectrums of distinct classes in classifications, is 0.1 [52]. Adopting the range of SA $\leq$ 0.1 as too small for two classes to be distinguishable, most individual classes in AncE appear distinct, with the exception of ParoA with SandB and CarpE with ArteC (Figure 4a). Contrastingly, most classes appear highly mixed in TavW (Figure 4b), with spectral affinity for (a) AmmoA with AnthM, CarpE, and HeliI; (b) AnthM with AmmoA, CarpE, CrucM, and ThymC; (c) CarpE with AmmoA, AnthM, and CrucM; (d) CrucM with AnthM, CarpE, ErynM, and HeliI; (e) DeadV with OtanM; (f) ErynM with CrucM; (g) HeliI with AmmoA and CrucM. Only classes ArteC, CladF, and SandB show high SAs throughout all classes. These relationships are investigated further by using the same multispectral data to train and test a hard RF classifier.

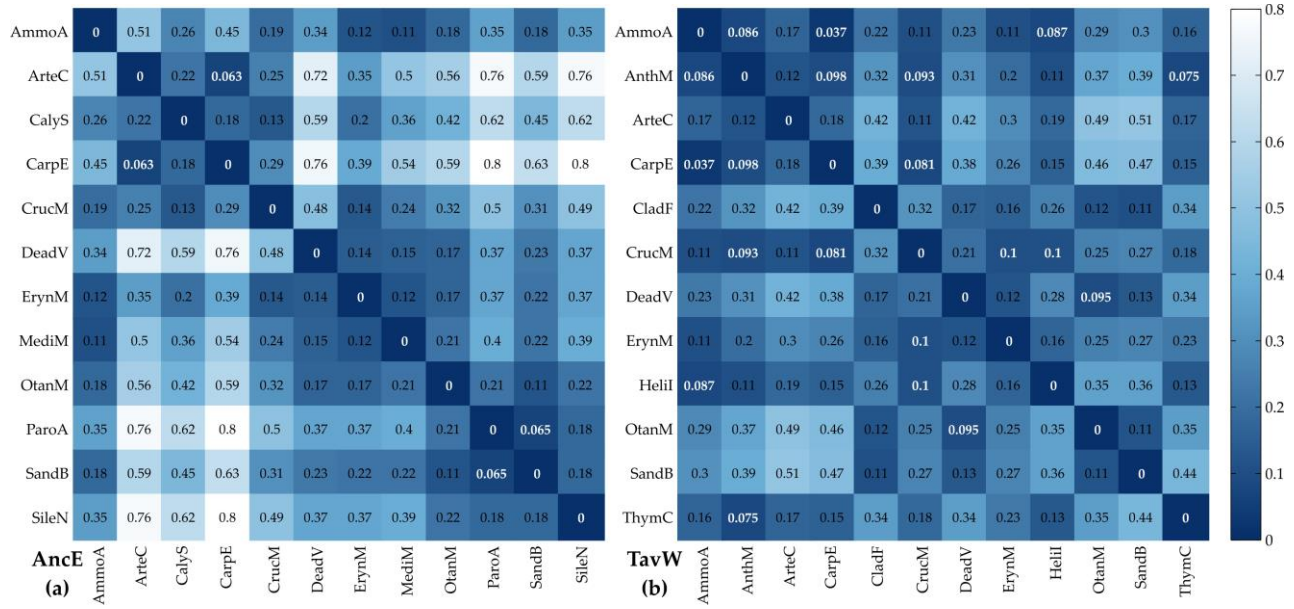

Figure 4. Heatmap of the Spectral Angle (SA, in radians; see Equation (3)) for AncE (**a**) and TavW (**b**), as an indicator of similarities and differences between the spectra of each class (values of SA $\leq$ 0.1 are given in bold white font).

3.2.2. Hard RF Classification

Hard classification approaches, as discussed previously, are practically inapplicable for mid-latitude dune systems, like the ones in Ria Formosa, due to the high spatial variability, the mixing of plant species, and the presence of species with very small plant parts. The hard RF classifier is applied here, not as a viable remote sensing methodology for the study

area, but to assess its ability to differentiate between species spectra at the original image resolution (i.e., prior to upscaling—spatial averaging—at the WV resolution).

The spectral data collected from individual pixels of the P4M were introduced to the RF hard classifier, maintaining, where possible, a relative balance in the presence of each class within the training population. The confusion matrix of the classification is given in Figure 5a for AncE and in Figure 5b for TavW, as values normalised by the true number of elements in each class; diagonal elements, therefore, correspond to the producer accuracy (complementary to the omission error) for each class. The overall accuracy of the classification is 0.78 and 0.85 for AncE and TavW, respectively, and Cohen's kappa score [53] is 0.77 and 0.83. Producer and user accuracies and omission and commission errors are shown in Figure 5c for AncE and Figure 5d for TavW, with the two sets generally showing similar values between the training and test populations. An exception is CarpE, with a significantly higher user than producer accuracy for both barriers (e.g., 0.95 versus 0.5 in AncE) and SileN (0.92 versus 0.24) and OtanM (0.86 versus 0.58) in AncE. High producer accuracy ($\geq$0.85) was obtained for classes (a) SandB and DeadV for both barriers, (b) ArteC, CalyS, CrucM, ErynM, and ParoA in AncE, and (c) CladF, HeliI, and OtanM in TavW. This provides further indication that the spectral signature of these classes should be distinct within the sample. The accuracy for MediM in AncE and AmmoA, AnthM, ArteC, CrucM, and ErynM in TavW could also be considered acceptable (>0.7), while spectral unmixing likely cannot be successful for the remaining classes.

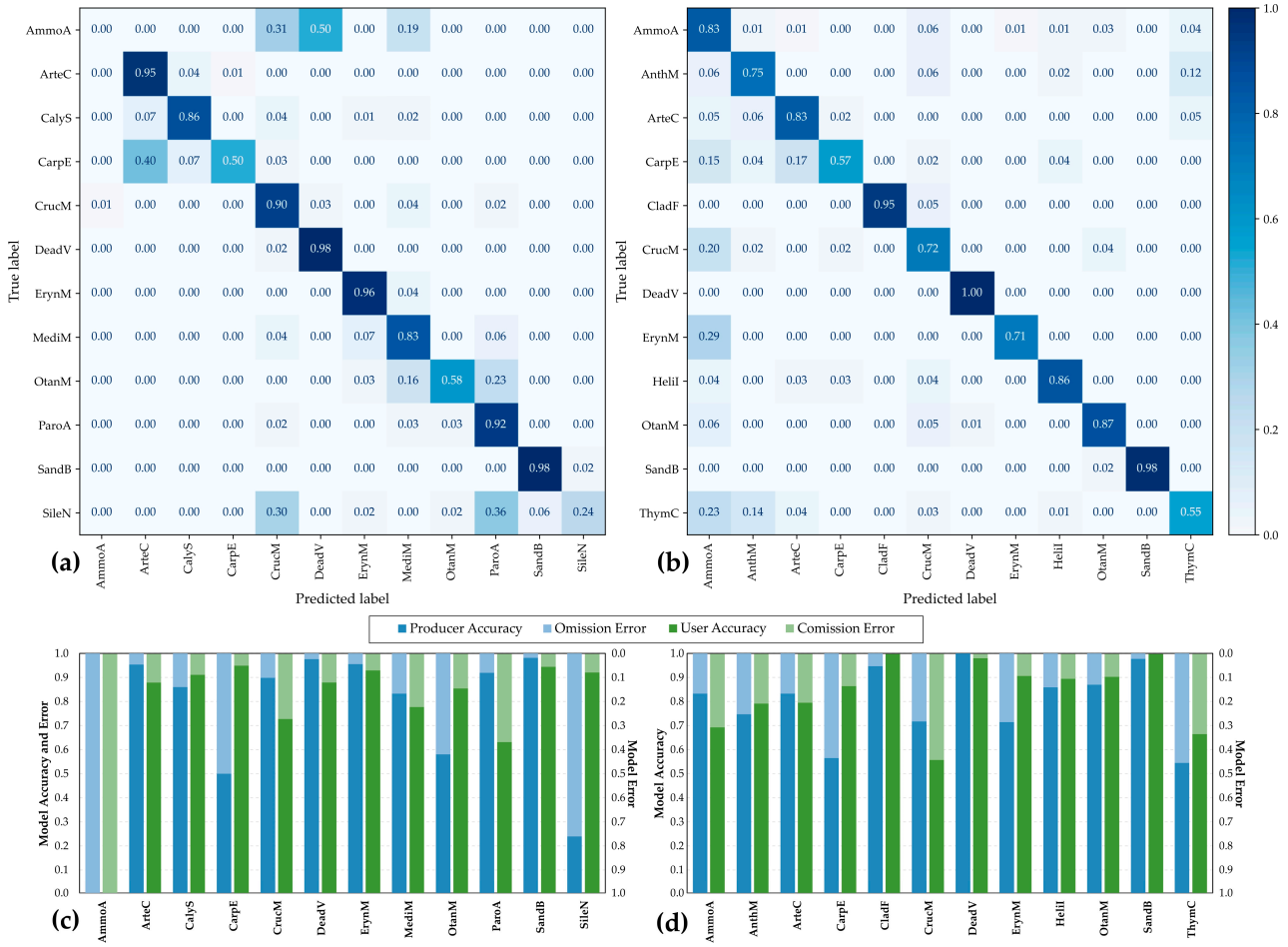

Figure 5. Confusion matrices (values normalised by the true number of elements in each class; the sum of each line equals to 1) and model accuracies and errors (left and right vertical axes, respectively) for AncE (**a**,**c**) and TavW (**b**,**d**) for the hard RF classification using pixel values of the drone multispectral bands as features.

It follows that some of the plant species may need to be grouped to improve model skill. Based on the producer accuracy from the tests in AncE, AmmoA (which showed a staggering error of 1) will likely need to be grouped with DeadV, and CarpE with ArteC, while for OtanM the hard classification indicates potential grouping with ParoA. In TavW, ThymC was mainly misclassified as AmmoA; AnthM and CarpE were misclassified as ArteC. In the applications of the RFR algorithms for spectral unmixing, we initially focus on assessing the skill of the model of classes prior to grouping while the potential for improving skill through species groups is investigated at a later stage (results shown in Table A1).

3.3. Spectral Unmixing Using RFR

3.3.1. RFR with UAV Data

The FC accuracies (CoD and RMSE), predicted by the RFR algorithm for each class (16 species of Table 2; 13 (11 plant species and DeadV and SandB) classes per plot) are shown in Figure 6 for AncE and TavW. Additionally, the corresponding mean absolute error (MAE) values are given in Table A2. The results refer to regressions considering both the entire plot area and only the foredune ridge, with skill indicators calculated from the regression results for the testing population. The number of pixels used for the training and testing are given in Table 2.

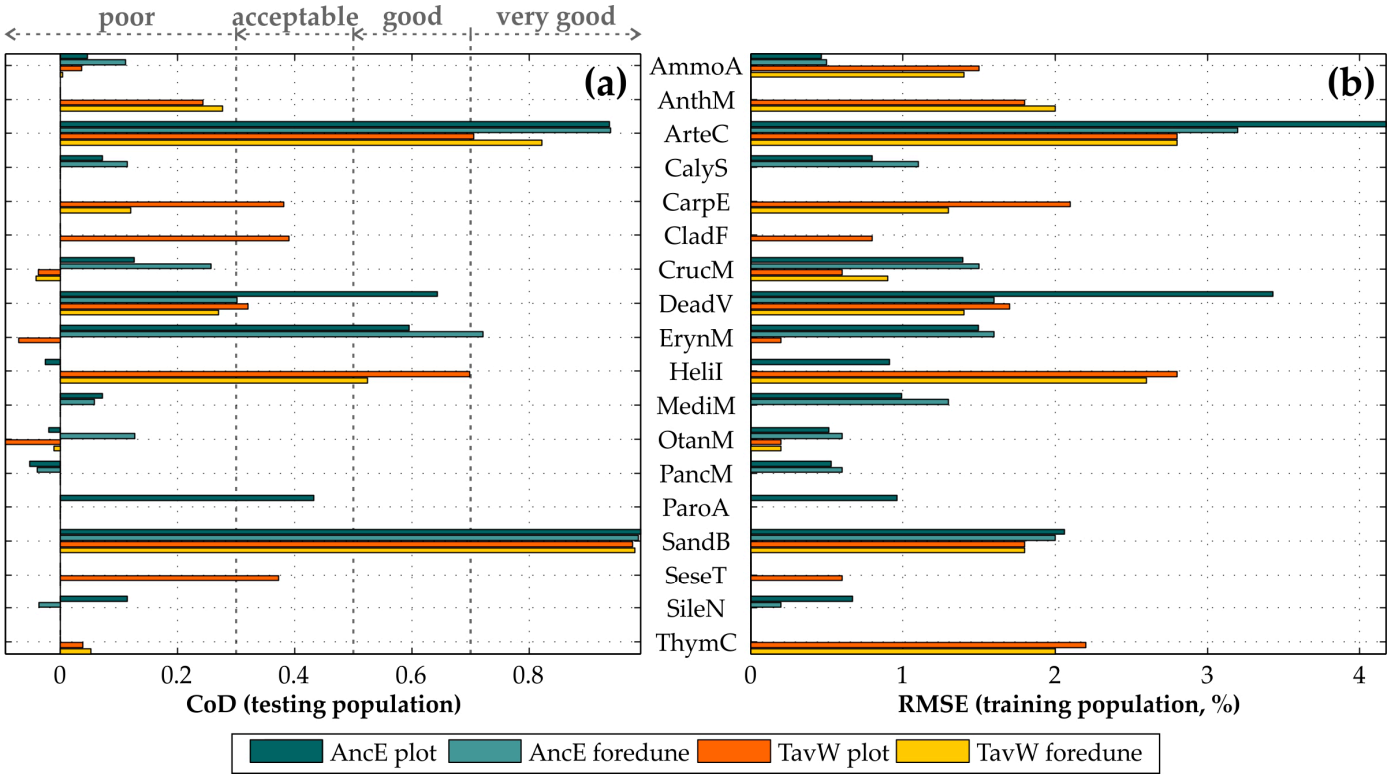

Figure 6. Accuracy metrics ((**a**) coefficient of determination (CoD (the evaluation scale is after Nikoo et al. [54]) and (**b**) root mean square error (RMSE)) for the UAV RFR tests, considering the entire AncE and TavW plots and only the foredune zones.

The model achieves near-perfect accuracy for the bare sand class (SandB: CoD~1, RMSE~2%, and MAE~1%) in all regressions (both domains and for the entire dune and foredune ridge zones). The linear model used for the estimation of FC_{veg} was applied to the high-resolution R and NIR bands of P4M (Equation (1)) and not to the upscaled feature data. Therefore, the success of the model is not due to forced linearity between independent and dependent values, and provides confirmation of the separability of the sand class by

the RFR model. This is also reinforced by the spectral analysis performed and the hard RF classification results, both supporting the separability of the class.

The RFR shows very good prediction skill for bushy vegetation like ArteC, with slightly better accuracy in AncE than in TavW, due to the higher expansion of the species in the domain (see Table 1) and higher spectral mixing with other species (producer accuracy of 0.83 in TavW and 0.95 in AncE; Figure 5). It should also be noted that ArteC is the class with the highest prediction RMSE, which is most likely related to the high variability of FC values in the domain (see Figure 3a).

Unsurprisingly, plant species abundance appears to be a critical factor for the model. For example, ErynM is sensed with good accuracy in AncE and especially over the foredune ridge (CoD~0.7), where it is most abundant, while the model shows no skill for TavW where the species is less common. Similar observations can be made for CrucM and DeadV, with better model performance in AncE than in TavW, where the classes are less dominant. HeliI was predicted with good overall accuracy (CoD~0.5 over the foredune and 0.7 for the entire plot) in TavW where the plant is highly abundant (Table 2 and Figure 3b) and showed negative CoD values in AncE, due to the low representativity of the species in the field. Similarly, CarpE and CladF were predicted with reasonable accuracy in the back dune of TavW (species absent in the foredune ridge; Table 1). ParoA, abundant over the back dune in AncE, was also sensed with acceptable accuracy.

Contrastingly, the FC of SeseT was predicted with acceptable skill, despite its very low presence in the back dune of TavW (Table 1; species absent in foredune). This is likely related to the bushy morphology of the plant and its distinct spectral signature. The model skill for CalyS was poor, despite its high abundance in the foredune of AncE and the relatively high producer accuracy in the hard RF classification (Figure 5a), which is potentially linked to its small plant size. The same is true for SileN, present most prominently in the back dune of AncE. In this case, however, the hard RF classifier also failed to separate the species (Figure 5a). Lastly, the RFR algorithm could not distinguish the species ThymC, AmmoA, PancM, MediM, and OtanM in the either of the plots (CoD < 0.1). For ThymC, a plant present throughout TavW (Table 2), spectral unmixing was unsuccessful due to spectral affinity with other classes (Figure 5b), namely with AnthM (Figure 4b). For the four other species, the failure is likely due to the combination of the low expansion of the plants in the domain, their morphologic characteristics (e.g., narrow stems and small leaves of AmmoA, OtanM, and MediM) and spectral signature.

The integration of different species in groups, based on the results of the preceding spectral analysis (Section 3.2), as an option to improve model skill, was also investigated. The results, provided in Appendix A, show a small gain in CoD compared to the best performing species prior to grouping (e.g., the group of AnthM and ThymC showed a CoD of 0.28, whereas AnthM had a CoD of 0.244; see Table A1). Therefore, seeing that grouping does not essentially improve model skill, the original classes are maintained for consistency in the remainder of the analysis.

The efficiency of other regressors, namely SVM and histogram gradient boosting, was also tested with the UAV data, with the skill of RFR being comparable, if not superior, to the other model results (Table A3). Moreover, a test was performed to identify the influence of spatial resolution to the RFR model results by reducing the pixel area to 1/25th (from 0.5 × 0.5 m to 0.1 × 0.1 m). The results did not show a clear pattern, with the higher spatial resolution RFR showing a higher CoD (by ~0.1) for AnthM and ThymC and a lower CoD (by ~0.1) for ArteC, DeadV, CladF, and SandB (Table A3). It follows that the smaller pixel size worsened the skill for the most abundant and better sensed classes in the original, coarser, prediction. This outcome was rather unexpected and draws attention

to the influence of spatial scale in the performance of spectral unmixing algorithms for future research.

The potential of improving the regression results by including morphological (distance to shoreline) and topographical (elevation from the DSMs) data as additional features to the five multispectral bands of the UAV was also tested. The results (Table 3) show that there was noticeable improvement in the model accuracy for AmmoA, CladF, CrucM, OtanM, and DeadV, even though some classes (e.g., OtanM) still showed very low skill. Comparing the CoD improvement between the tests with six and seven features (considering only the distance to shoreline and both parameters, respectively; Table 3), it becomes clear that the distance to the shore was the main contributor to the improvement, while including elevation resulted in an additional increase in CoD that ranged between 8% (for OtanM) and 40% (for CrucM and DeadV).

Table 3. Comparison of CoD (testing population) for TavW and all classes, using five (the P4M multispectral bands), six (the 5 P4M bands + distance to shoreline) and seven features (the 5 P4M bands + distance to shoreline + elevation), and CoD difference, showing the improvement (positive values ≥ 0.1 are formatted in bold) by the inclusion of the additional features, compared to solely multispectral UAV data; differences in RMSE were low (<0.5%) and were omitted for brevity.

Class	CoD			CoD Difference	
	$N_{features} = 5$	$N_{features} = 6$	$N_{features} = 7$	[6-5] *	[7-5] *
AmmoA	0.037	0.331	0.365	**0.294**	**0.328**
AnthM	0.244	0.295	0.314	0.051	0.070
ArteC	0.706	0.797	0.781	0.091	0.075
CarpE	0.381	0.411	0.430	0.030	0.049
CladF	0.390	0.530	0.581	**0.140**	**0.191**
CrucM	−0.037	0.046	0.079	0.083	**0.116**
DeadV	0.320	0.447	0.497	**0.127**	**0.177**
ErynM	−0.071	−0.132	−0.138	−0.061	−0.067
HeliI	0.699	0.753	0.761	0.054	0.062
OtanM	−0.094	0.105	0.120	**0.199**	**0.214**
SandB	0.977	0.978	0.978	0.001	0.001
SeseT	0.373	0.378	0.362	0.005	−0.011
ThymC	0.039	0.041	0.044	0.002	0.005

* [6-5] and [7-5] refer to the the CoD of test $N_{features} = 6$ minus the CoD of test $N_{features} = 5$ and to the CoD of test $N_{features} = 7$ minus the CoD of test $N_{features} = 5$, respectively.

The accuracy of the RFR models, trained in AncE and TavW, was also tested with unseen data from AncW and TavE (see Figure 1 for location), respectively. The results are given in Figure 7 and focus on five classes in each plot that showed acceptable or higher skill in the testing populations (i.e., CoD > 0.3 in Figure 6). The CoD in AncW exceeds 0.6 for all five main classes, with low RMSEs (below 0.03). For TavE the model skill is lower, but overall comparable to the training plot of TavW. Only for the bare sand class is the performance significantly lower (CoD 0.63 versus 0.98). RMSEs are also higher than AncW, reaching 0.85 for SandB. Overall, the trained RFR models maintained their predictive capacity, performing well with out-of-sample data from the same barrier, indicating a low risk of overfitting and confirming the robustness of the models and the reliability of the predictions of the major classes for real-world applications.

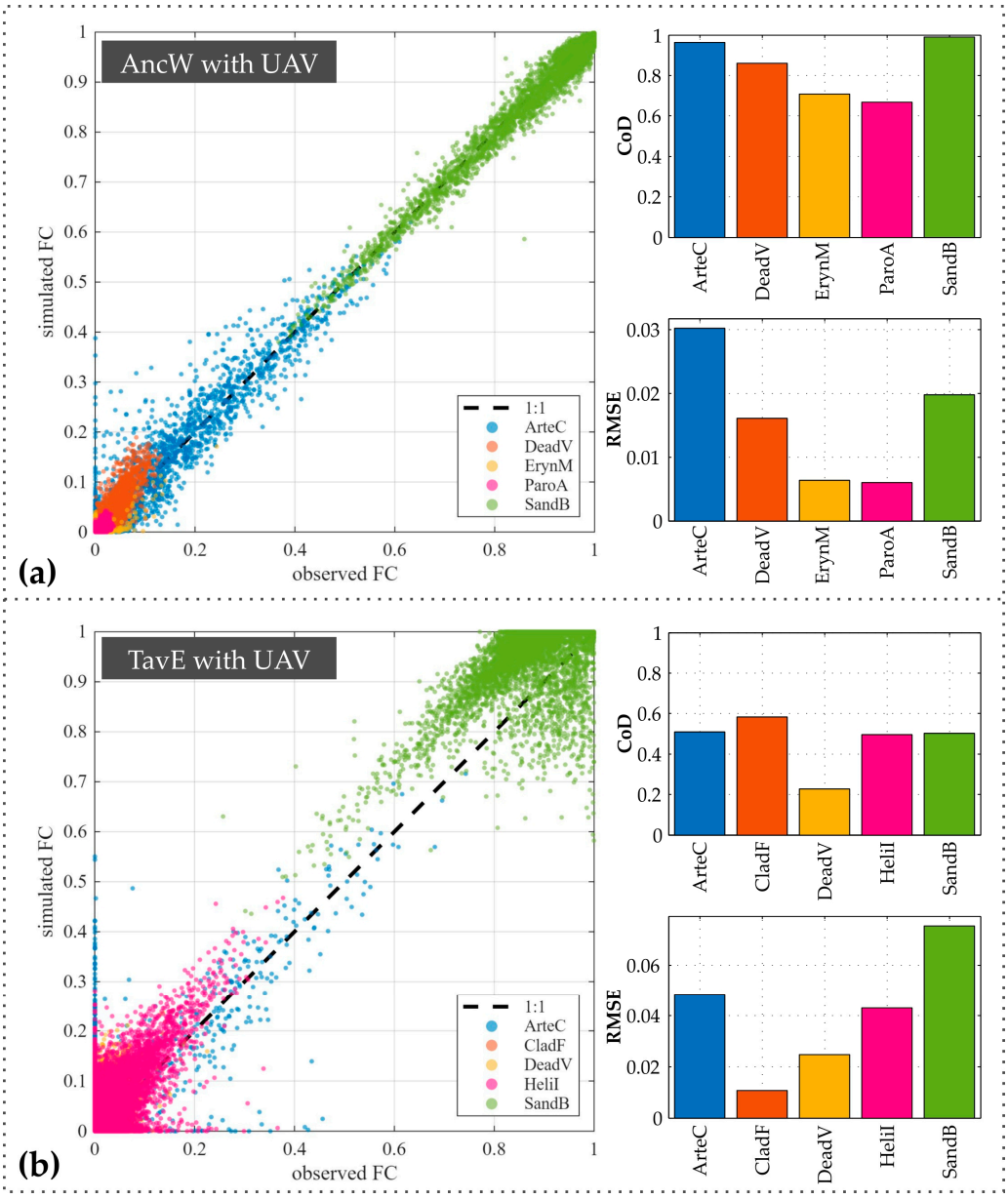

Figure 7. RFR results using unseen UAV data from the plots of AncW (**a**) and TavE (**b**): scatterplots of observed versus simulated FC and bar plots of CoD and RMSE for classes that showed reasonable skill in AncE and TavW (CoD $\geq$ 0.3 for $N_{features}$ = 5 in Table 3).

3.3.2. RFR with WV2 Data

The target dataset was combined with the feature dataset comprising the surface reflectance values from the eight WV2 bands (Figure 2) to train and test models for AncE and TavW. The same hyperparameters as for the UAV application were applied. The CoD and RMSE values for the testing population, considering only the foredune and the entire dune plots, are given in Figure 8 (a and b, respectively; MAEs are given in Table A2). The number of pixels used for the training and testing can be found in Table 2.

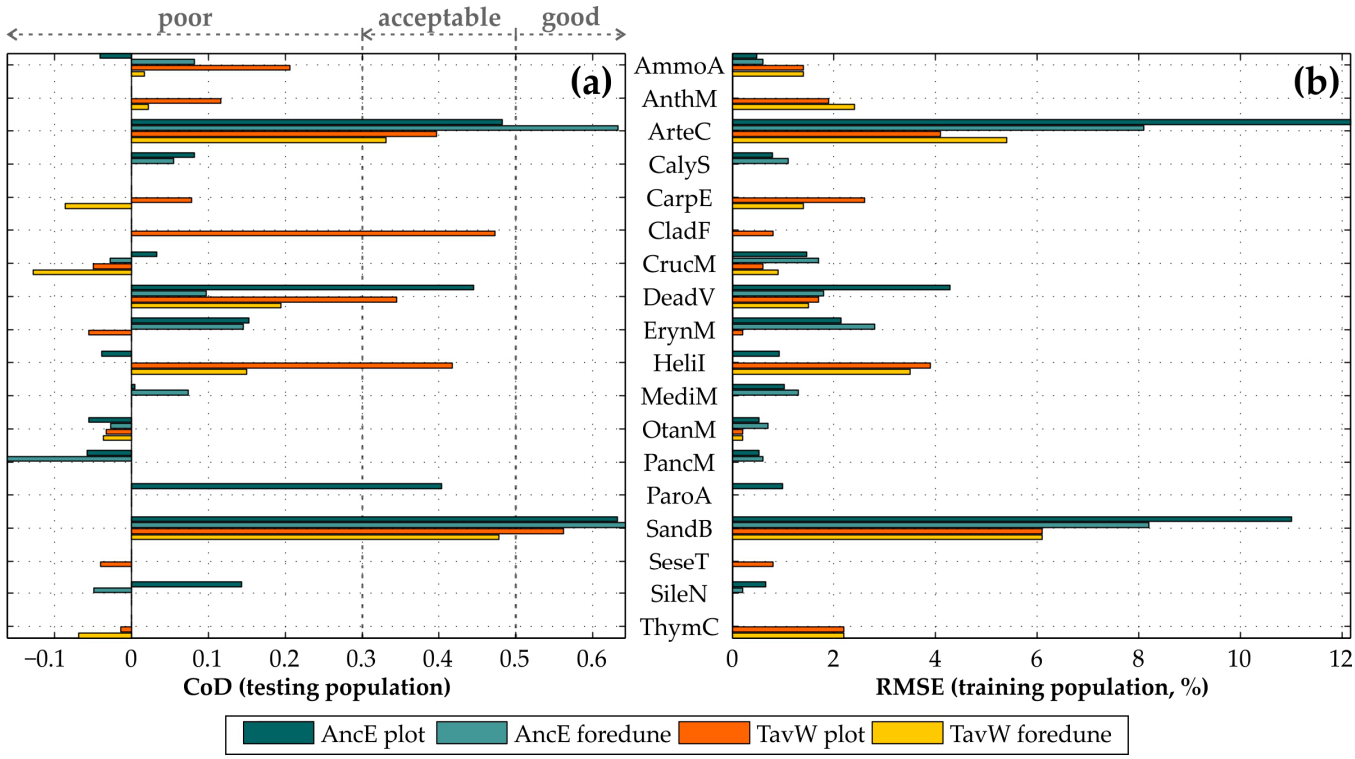

Figure 8. Accuracy metrics ((**a**) coefficient of determination (CoD (the evaluation scale follows Nikoo et al. [54]) and (**b**) root mean square error (RMSE)) for the WV2 RFR tests, considering the entire AncE and TavW plots and only the foredune zones.

The accuracy metrics show the same tendencies with respect to the classes as for the UAV application, with ArteC and SandB being the best performing classes for both barriers, while for AncE, ParoA, and DeadV also show acceptable skill. In TavW, the model captures the presence of CladF, DeadV, and HeliI over the back dune with acceptable accuracy (except HeliI in the foredune, showing low CoD). The RMSEs (and MAEs; Table A2) are elevated for ArteC and SandB in AncE, which are the most abundant classes in the area and the ones showing the highest variability in FCs (see Figure 3b). As was the case with model application using UAV multispectral data, species grouping for the application with WV2 data also showed that CoD values improved only slightly, compared to the best performing class within the group (see Table A1).

Overall, the skill of RFR for the WV2 data is strongly reduced, compared to the predictions with UAV data, despite the higher spectral resolution of the former (eight bands versus five bands). Considering the classes with acceptable and better model skill for the UAV application (Figure 6), we note a loss in skill (CoD_{WV2}-CoD_{UAV}) of 0.35 to 0.39 for SandB, 0.31 to 0.46 for ArteC and 0 to 0.2 for DeadV in the two plots, of 0.45 for ErynM and 0.03 for ParoA, and of 0.29 for HeliI in TavW; interestingly, the skill of WV2 is slightly better for CladF in TavW, showing a skill gain of 0.08, potentially thanks to the higher spectral resolution. It needs to be stressed that the lower skill of the RFR using WV2 is mainly related to the predicted FC value of the class, whereas the algorithm was quite accurate in predicting the location of classes. Visually effective representation of this capacity through maps is difficult due to the size of the plots and the low FC and absolute error (e.g., observed—predicted) values. Instead, to visualise the capacity of the model to accurately pinpoint the location of classes, model predictions (and observations) were translated into binary confusion matrices for each class, expressing correct and incorrect predictions on the class presence (and absence) in each WV2 pixel. This analysis, along with related performance metrics, is included in Appendix A.3. The results show that RFR

effectively detects true instances (low false negatives), while it mainly misclassifies plants (high false positives) in classes where accuracy was also low using P4M data (e.g., AmmoA, CarpE, CrucM, SeseT, and ThymC).

As in the UAV tests, the introduction of distance to the shoreline and elevation data as additional features was also tested for the WV2 multispectral data. The differences in CoD by the addition of morphological information (only adding the distance from shoreline ($N_{features}$ = 9) and adding both parameters ($N_{features}$ = 10), compared to the eight multispectral bands ($N_{features}$ = 8)) in TavW are given in Table 4. RMSE variability was low, and the values are omitted for brevity. The CoD shows noticeable improvement in the classes of ArteC, CladF, and DeadV, while the increase for AmmoA was also relatively important. Interestingly, model skill reduced for the classes of ErynM and SeseT. Again, the inclusion of elevation data did not translate to significant improvement compared to the results obtained using only the distance to shoreline. It follows that the low gain in model skill probably does not justify the need for elevation information, whereas the distance to the shoreline can improve results in some of the classes.

Table 4. Comparison of CoD (testing population) for TavW and all classes, using 8 (the WV multispectral bands), 9 (the 8 WV bands + distance to shoreline) and 10 bands (the 8 WV bands + distance to shoreline + elevation) and CoD difference, showing the improvement (positive values $\geq$ 0.1 are formatted in bold) by the inclusion of the additional features, compared to solely multispectral WV data; differences in RMSE were low (<0.5%) and were omitted for brevity.

Class	CoD			CoD Difference	
	$N_{features}$ = 8	$N_{features}$ = 9	$N_{features}$ = 10	[9-8] *	[10-8] *
AmmoA	0.206	0.287	0.302	0.081	0.096
AnthM	0.116	0.134	0.156	0.018	0.04
ArteC	0.397	0.531	0.556	**0.134**	**0.159**
CarpE	0.078	0.152	0.168	0.074	0.09
CladF	0.473	0.581	0.634	**0.108**	**0.161**
CrucM	−0.05	−0.044	−0.025	0.006	0.025
DeadV	0.345	0.487	0.509	**0.142**	**0.164**
ErynM	−0.056	−0.103	−0.34	−0.047	−0.284
HeliI	0.417	0.462	0.505	0.045	0.088
OtanM	−0.033	−0.013	0.012	0.02	0.045
SandB	0.562	0.6	0.63	0.038	0.068
SeseT	−0.04	−0.089	−0.096	−0.049	−0.056
ThymC	−0.014	−0.005	0.018	0.009	0.032

* [9-8] and [10-8] refer to the CoD of test $N_{features}$ = 9 minus the CoD of test $N_{features}$ = 8 and to the CoD of test $N_{features}$ = 10 minus the CoD of test $N_{features}$ = 8, respectively.

Applying the trained RFR models to the unseen WV2 data of AncW and TavE (Figure 9) produced comparable accuracies for the five detectable classes for each plot (the same five classes as for the application with unseen P4M data) to the ones obtained for the training and testing dune plots with WV2 (Figure 8). CoD was even slightly better (by around 0.1 to 0.2) than the test score in AncE for classes SandB, DeadV, and ParoA and in TavW for classes ArteC and CladF. DeadV and SandB in TavE, on the other hand, showed lower CoD values than in TavW (by 0.06 and 0.11, respectively). The overall consistency in performance, as was the case for the predictions with unseen P4M data, indicates that the model is not overfitted and maintains its predictive accuracy well beyond the training dune plot, supporting the reliability of RFR predictions using WV2 for the main detectable classes.

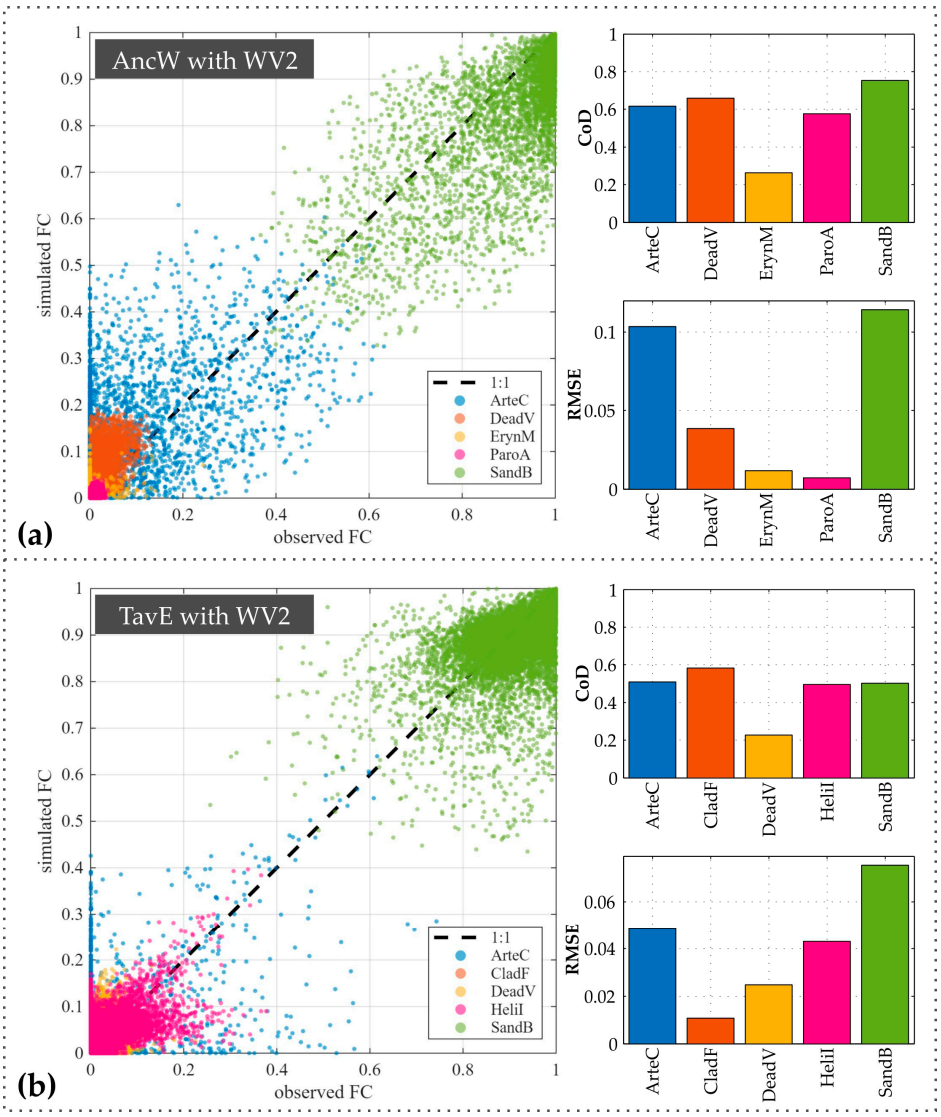

Figure 9. RFR results using unseen WV data from the plots of AncW (**a**) and TavE (**b**): scatterplots of observed versus simulated FC and bar plots of CoD and RMSE for classes that showed reasonable skill in AncE and TavW (CoD $\geq$ 0.3 for $N_{features}$ = 8 in Table 4).

4. Discussion

Spectral unmixing approaches have been successfully applied in remote sensing of habitats with higher FCs (e.g., marshes; [28]). In fact, the RFR algorithm applied herein has been used to predict plant FC distribution in the North Inlet–Winyah Bay saltmarsh (Georgetown, SC, USA) using UAV and WV2 data [29]. The model (called a rescaled RFR in the work of Yang et al.) was able to accurately estimate the FC of bare soil and two dominant marsh species (0.57 < CoD < 0.93 and 0.05 < RMSE < 0.27) but did not capture the distribution of a less dominant species effectively [29]. Our application of the same approach in the highly mixed coastal dunes of the Ria Formosa barriers led to similar results and observations regarding model skill and limitations. The model was able to predict the FC of five major classes in the two barrier islands tested (three plant species, SandB, and DeadV), with reasonable-to-very good accuracy using upscaled UAV data (0.39 < CoD < 0.99 and 0.018 < RMSE < 0.041) and with reasonable-to-good accuracy using WV2 data (0.35 < CoD < 0.62 and 0.040 < RMSE < 0.123). Class expansion is an important factor, with dune plant species present in less than around 1/5th of the pixels (see Table 2) being practically undetectable. This may be linked to the FC distribution

within the sample, as an imbalanced dataset typically leads to underprediction of minority classes within the model population [55]. Still, resampling approaches that target this imbalance by artificially reinforcing the presence of 'rare' data within the distribution, such as the Synthetic Minority Oversampling Technique for Regression (SMOTER; [56]), did not improve skill with underperforming classes for TavW with WV2 (see Table A3). More specifically, an adapted version of SMOTER [56] was applied, that accounts for the prevalence of zero-FC observations for minority plant classes in our dataset (see Figure 3) by considering only the non-zero value distribution to both (a) identify the rare values (instances that exceeded the mean plus the standard deviation of non-zero FCs of the class) and (b) perform the oversampling (using k-nearest neighbour interpolation within the rare values and oversampling rare values with a factor of 5). Therefore, the detection failure is most likely a combination of the low representation of some classes, combined with plant characteristics. Especially for plants whose aboveground parts cover a low proportion of the WV pixel, their signal is most likely overwhelmed by other classes that cover more space over the pixel, even if their spectral signature is distinct. An example is CalyS that, despite appearing spectrally distinct from the remaining classes while using native resolution UAV multispectral data (high SA throughout (Figure 4a) and an accuracy of 0.87 in the hard RF (Figure 5a)), showed very poor skill in tests using data from larger pixel sizes (upscaled P4M at 0.5 m and WV2).

Compared with other spectral unmixing regressor models tested, RF performed better than SVM and HGB for predicting FC at the subpixel level in the Ria Formosa coastal dunes. Contrastingly, Medina Machín et al. found hard SVM classification outperforming linear unmixing for the identification of six non-herbaceous plant species (five shrubs and one rush) in the Maspalomas dunes (Grand Canaria Island, Spain) from WV2 imagery [7]. The size of these plants typically exceeds the WV2 pixel, indicating that the application of unmixing techniques was likely not strictly necessary and therefore justifying the higher accuracy of hard classifiers. It follows that the target species in the Maspalomas dunes were significantly different than our study, with only some of the ArteC plants in Ria Formosa reaching similar sizes. Similarly, the size of the target classes, compared to the spatial resolution of the features used, is an important consideration for the observations of Pafumi et al. regarding the skill of hard and soft RF classifiers for coastal dune habitat identification from WV3 (in two sites in Tuscany, Italy) [32]. The authors concluded that hard approaches were better at classifying dune scrubs and white dunes, while also noting that soft approaches captured a more realistic representation of vegetation patterns [32]. These considerations and observations highlight the importance of selecting a level of analysis aligned with the objectives of each study site and case. Whereas, for example, hard approaches may be more accurate for the identification of coastal dune habitats, they are hardly justifiable for satellite observation of dune species in highly mixed systems.

The spatial resolution of the feature dataset can impact the model skill, as evidenced in the reduced performance of RFR using PS imagery (see Appendix A.4). Ettritch et al. also found an exponential increase in total dune vegetation abundance error with decreasing spatial resolution [31]. However, the RFR tests comparing UAV multispectral data resampled at 10 cm and 50 cm pixels did not follow this pattern, with the higher resolution slightly underperforming in terms of the most abundant classes. Smyth et al. also noted higher errors occurring when applying supervised classification to very high image resolution multispectral UAV data (e.g., for a 0.01 m versus a 0.25 m pixel size) [49]. A systematic approach, aiming to study the combined impact of spatial resolution and the predominance of one class with respect to the others on the unmixing accuracy is needed to provide more clarity on these influences.

The assessment of potential improvement in model skill by the inclusion of morphological data in the predictor dataset showed that the distance to the shoreline was more effective, increasing model skill by 7 to 40% when using UAV data and by 10 to 55% when using WV2 data. Lansu et al. also observed accuracy improvement, albeit accompanied with a small decrease in precision, in dune habitat mapping using Convolutional NN along the Dutch coast after including the distance to shoreline to coarse (25 cm) UAV multispectral data [19]. Their results improved further by also including elevation data (digital surface model and canopy height), which was mostly linked to a better separation between shrubs and broadleaf trees [19]. Similarly, Franklin et al. reported a 90% accuracy in detecting the presence of shrubs in the barrier islands of Virginia (USA) from LandSat-LiDAR imagery composites, using decision trees and RFs [57]. Other works, like that of Cruz et al. who used RF with UAV data [12], also advocate for the inclusion of elevation data for dune habitat monitoring. We found that the additional skill enhancement was too low to justify the need for topographic data (obtained by DEM and resampled at 0.5 m), even for applications only considering the embryonic dune and the foredune ridge, where topography is more linked to species distribution (e.g., [33]). In coastal dune systems, however, where elevation is an important model predictor for dune plant distribution, spectral unmixing could be applied jointly with novel approaches for achieving reasonable accuracies (0.5–1 m) in satellite-derived DEMs (e.g., [58]) for coastal observation and monitoring through satellite imagery.

The grouping of dune plant species based on spectral similarities was performed as an exercise in improving model accuracy and showed that each group essentially adopted the skill of its the best-performing member, without notable additional gains. While grouping did not essentially improve accuracy for our system, it needs to be stressed that some of the species that were included within a 'spectrally similar' group do not belong to the same successional stage type (e.g., AmmoA is a dune builder and should not have been grouped with sand-binder species like CrucM, ErynM, and OtanM; see [59]). Such considerations, along with the location of plants within the dune system, need to be considered, especially in highly mixed dune systems. Hyperspectral imagery, on the other hand, could provide critical missing spectral detail needed to improve the segregation of plants or plant groups. Laporte-Fauret, for example, obtained good accuracies using RF classification of airborne hyperspectral imagery (spatial resolution: 1 m; spectral resolution: 4.5 nm; spectral range: from 409.23 to 987.08 nm) to classify nine plant species in a coastal dune system in southwest France, but noted a reduced model skill for small plants and low-density vegetation patches (i.e., mixed pixels) [14]. Their results were limited by the low spatial resolution, combined with the pixel-by-pixel approach employed, whereas our results were likely mostly limited by the available spectral resolution.

It follows that coupling spectral unmixing algorithms with hyperspectral imagery could be the key to overcoming these limitations and appears to be a promising direction for future research in Earth observation of coastal dunes. Combining such data with automated (e.g., object-based classification [15]) or semi-automated (e.g., [60]) segmentation tools to delineate individual classes or class groups would significantly decrease the manual labour involved in compiling the reference dataset. Additionally, FC_{veg} can be estimated using a subset of the ground truth data and machine learning methods, like RFs that showed high accuracy in predicting the FC of desert vegetation [46]. Such avenues could increase the automation and robustness of the approach, paving the way to wide-scale monitoring applications. At the same time and considering the good model skill in terms of sensing the FC of bare sand (or total vegetation) and major plant species from both drone and satellite imagery, such products can be capitalised on in coastal dune environmental research. For example, spectral unmixing results can (a) be incorporated into aeolian sand transport

models to inform on plant distribution in the field, thus making it possible to improve approximations of flow–plant interactions (e.g., reducing flow velocity with vegetation cover [61]) and predictions of dune morphological change; (b) be used to monitor sand cover as an indicator of dune mobility (e.g., mapping of blowouts [62]); or (c) be used to monitor dune vegetation cover as indicator of dune vulnerability (e.g., using FC_{veg} thresholds [63]).

5. Conclusions

The main conclusions drawn from the analysis performed are as follows:

- Spectral unmixing algorithms, like the subpixel random forest regressor, can achieve good accuracies in detecting the fractional cover of major species (most abundant classes and bushy vegetation) in Mediterranean dune environments using multispectral data from coarse UAV flights or high-resolution satellites. The model showed poor skill in detecting small-stemmed or less abundant plant species in the domain (i.e., present over less than 5% of the pixels). Random forest achieved better accuracies than support vector machine and histogram gradient boosting regressors.
- Our results point to class abundance and plant characteristics (the area of plant cover within the satellite image pixel, along with spectral signature) being a significant limiting factor for the detectability of a class. Species with distinct spectral properties but low representation within the WV pixel (e.g., *Calystegia soldanella*) were not detectable, and neither were species with a high presence in the field and cover within the WV pixel, but without strong spectral differences (e.g., *Thymus carnosus*).
- The trained model demonstrated strong generalisation ability, as reflected in its good performance on previously unseen test data. This suggests that the model effectively captured the underlying patterns in the plant distribution rather than noise or overfitting to the training distribution. The robustness of the trained RFR for the selected classes indicates that it can provide reliable predictions of major dune plant species in sparsely vegetated dune environments with reasonable accuracy for real-world applications, such as large-scale monitoring.
- Grouping of species with respect to their spectral signatures resulted to very small increase in skill compared to the best performing species within each group, for both dune sites and multispectral data (UAV and WV2) tested. It follows that grouping did not improve performance in our study site; however, it should be stressed that the grouping of plant species in dune systems should not only consider the spectral properties of plants, but also their biogeomorphic characteristics (e.g., functional traits: pioneers, dune builders, and sand-binders).
- The analysis performed in Ria Formosa shows that the accuracy of spectral unmixing through random forest regressors can be enhanced by including morphological data in the predictor dataset. By including the distance to the shoreline, an increase in the coefficient of determination of around 0.1 was obtained for most major classes, while including elevation data led to a further increase in the order of 0.02–0.05. The influence of elevation is deemed to be too low and likely does not justify the need to obtaining elevation data, especially for the purposes of large-scale, systematic monitoring.
- Enhancing the broadness and resolution of the spectral data used with unmixing algorithms may be the key to improving the segregation of plants or plant groups in highly mixed coastal dunes, and is a research direction worth pursuing. In conjunction with automated segmentation tools for reference data extraction, spectral unmixing from super-/hyperspectral data could be a significant step forward in coastal dune observation.

Author Contributions: Conceptualization, K.K., S.C., Z.Y. and S.S.; methodology, K.K., S.C., J.B.G.-F., Z.Y. and S.S.; software, K.K. and Z.Y.; validation, K.K.; formal analysis, K.K.; investigation, K.K.; resources, K.K.; data curation, K.K., S.C., J.B.G.-F., L.B.d.S. and Z.Y.; writing—original draft preparation, K.K.; writing—review and editing, K.K., S.C., J.B.G.-F., Z.Y., L.B.d.S. and S.S.; visualisation, K.K.; supervision, K.K.; project administration, K.K.; funding acquisition, K.K. All authors have read and agreed to the published version of the manuscript.

Funding: This research was funded by the Fundação para a Ciência e a Tecnologia (FCT), Portugal, through grant 2022.06615.PTDC (DEVISE project; http://doi.org/10.54499/2022.06615.PTDC). K.K. was supported by the contract https://doi.org/10.54499/CEECINST/00146/2018/CP1493/CT0011; S.C. was supported by the contract https://doi.org/10.54499/CEECINSTLA/00018/2022/CP2967/CT0003; and L.B.d.S. was supported through the project https://doi.org/10.54499/2022.05392.PTDC, all funded by FCT. K.K., S.C., and L.B.d.S. also recognise the funding attributed by FCT to CIMA (https://doi.org/10.54499/UID/00350/2025) and to the Associate Laboratory ARNET (https://doi.org/10.54499/LA/P/0069/2020). Z.Y. was also supported by the Georgia Coastal Ecosystems Long-Term Ecological Research project, which is supported by the National Science Foundation (OCE-1832178). S.S. was supported by the RETURN Extended Partnership and received funding from the European Union Next-GenerationEU (National Recovery and Resilience Plan—NRRP, Mission 4, Component 2, Investment 1.3—D.D. 1243 2 August 2022, PE0000005).

Data Availability Statement: The WorldView (WV) satellite imagery and derived products used in this study are proprietary and were obtained under a commercial licence from Maxar Technologies. Due to licencing restrictions, these data cannot be shared publicly but may be obtained through Maxar Technologies (www.maxar.com; accessed on 21 June 2024) under similar licencing terms. UAV data supporting the conclusions of this article will be made available by the authors on request, while all algorithms used herein are openly available at https://scikit-learn.org/ (accessed on 9 July 2024).

Acknowledgments: The authors thank CIMA/ARNET for granting access to the P4M and M2P UAVs and RTK-DGPS used in the fieldwork. PlanetScope imagery was obtained through the European Space Agency (ESA) as part of its Third-Party Mission programme (Earthnet).

Conflicts of Interest: The authors declare no conflicts of interest.

Abbreviations

The following abbreviations are used in this manuscript:

AOI	Area Of Interest
CoD	Coefficient of Determination
DSM	Digital Surface Model
FC	Fractional Cover
GCP	Ground Control Point
M2P	Mavic 2 Pro
NDVI	Normalised Difference Vegetation Index
NIR	Near-Infrared
NN	Neural Network
P4M	Phantom 4 Multispectral
PS	PlanetScope
RGB	Red–Green–Blue
RF	Random Forest
RFR	Random Forest Regressor
S2	Sentinel-2
SA	Spectral Angle
SVM	Support Vector Machine
UAV	Unmanned Aerial Vehicle
WV	WorldView

Appendix A

The appendix includes additional plots and tables (Appendix A.1) and assessment of model sensitivity to RFR hyperparameters (Appendix A.2), performance metrics for the WV2 application, calculated after interpreting model FC predictions as binary confusion matrices for each class (Appendix A.3) and for the application using Planet-Scope imagery (Appendix A.4).

These data and analyses were included herein and not in the main manuscript body to provide additional information without interrupting the flow of the analysis.

Appendix A.1. Additional Tables and Plots

Table A1. Comparison of RMSE and CoD (testing population) in AncE and TavW (upper and lower parts, respectively) using P4M and WV2 data (left and right parts, respectively) for the initial application and after grouping species with respect to considering spectral similarity.

	P4M				WV2			
AncE	**RMSE**	**CoD**	**RMSE**	**CoD**	**RMSE**	**CoD**	**RMSE**	**CoD**
AmmoA	1.515	0.037	1.604	0.038	1.372	0.208	1.595	0.212
CrucM	0.618	−0.037			0.610	−0.062		
ErynM	0.204	−0.071			0.243	−0.059		
OtanM	0.205	−0.094			0.162	−0.036		
ArteC	2.897	0.706	3.018	0.747	4.126	0.395	4.897	0.35
CarpE	2.108	0.381			2.571	0.063		
SeseT	0.602	0.373			0.816	−0.048		
AnthM	1.834	0.244	2.534	0.279	1.901	0.11	2.908	0.081
ThymC	2.295	0.039			2.228	−0.019		
	P4M				**WV2**			
TavW	**RMSE**	**CoD**	**RMSE**	**CoD**	**RMSE**	**CoD**	**RMSE**	**CoD**
AmmoA	0.48	−0.017	1.736	0.191	0.486	−0.055	1.862	0.082
MediM	0.995	0.066			1.027	−0.006		
CrucM	1.403	0.117			1.469	0.025		
ArteC	4.097	0.941	4.02	0.942	12.165	0.48	12.262	0.477
CalyS	0.801	0.067			0.794	0.078		
ErynM	1.474	0.597	1.57	0.632	2.135	0.148	2.28	0.148
OtanM	0.518	−0.026			0.525	−0.071		
HeliI	0.914	−0.03	1.19	−0.041	0.918	−0.043	1.157	−0.043
PancM	0.534	−0.071			0.53	−0.064		
SileN	0.662	0.139	1.091	0.99	0.661	0.141	11.057	0.633
SandB	2.042	0.987			11.005	0.641		

Table A2. Mean absolute error (MAE; in %) of predicted class FC from RFR results using UAV and WV2 data in AncE and TavW; values correspond to the testing population.

Class	AncE				TavW			
	Plot		Foredune		Plot		Foredune	
	UAV	WV2	UAV	WV2	UAV	WV2	UAV	WV2
AmmoA	0.04	0.04	0.06	0.07	0.31	0.26	0.40	0.41
AnthM	-	-	-	-	0.94	1.07	0.84	1.02
ArteC	1.79	6.39	1.09	2.85	0.74	1.11	0.92	1.91
CalyS	0.19	0.19	0.36	0.37	-	-	-	-
CarpE	-	-	-	-	0.53	0.67	0.14	0.20
CladF	-	-	-	-	0.39	0.30	-	-
CrucM	0.23	0.27	0.33	0.45	0.09	0.09	0.22	0.24
DeadV	0.87	1.34	0.66	0.84	1.00	0.99	0.70	0.76
ErynM	0.34	0.55	0.52	1.02	0.01	0.01	-	-
HeliI	0.06	0.06	-	-	1.54	2.49	1.16	1.71
MediM	0.22	0.23	0.36	0.39	-	-	-	-
OtanM	0.04	0.05	0.06	0.07	0.01	0.02	0.03	0.04
PancM	0.06	0.07	0.07	0.08	-	-	-	-
ParoA	0.48	0.73	-	-	-	-	-	-
SandB	1.19	6.62	1.03	4.01	1.20	4.20	1.02	3.66
SeseT	-	-	-	-	0.02	0.02	-	-
SileN	0.25	0.37	0.02	0.03	-	-	-	-
ThymC	-	-	-	-	0.77	0.85	0.59	0.68

Table A3. Additional model runs in TavW (CoD values for the testing population), using: P4M data, where RFR 50 cm: RFR model results discussed in Section 3.3.1; HGBR: histogram gradient boosting regressor results (using loss = 'squared_error', max_iter = 300, max_leaf_nodes = 15, early_stopping = False, random_state = 0); SVMR: support vector machine regressor results (kernel = 'rbf', C = 100, epsilon = 0.01). RFR 10 cm: RFR model results, using P4M data with a pixel size of 10 × 10 cm (i.e., 1/25th of the RFR 50 cm pixel); RFR 50 cm, HBBR and SVMR use P4M data, upscaled at the WV pixel grid; and WV2 data, where RFR: model results discussed in Section 3.3.2; RFR SMOTER: minority values were reinforced in the training set, by oversampling values exceeding the mean plus one standard deviation of the non-zero FC values (following the SMOTER approach of Torgo et al., [58]).

Class	P4M Data				WV2 Data	
	RFR 50 cm	HGBR	SVMR	RFR 10 cm	RFR	RFR SMOTER
AmmoA	0.037	0.002	−0.394	−0.03	0.208	0.118
AnthM	0.244	0.258	0.199	0.341	0.110	0.110
ArteC	0.706	0.692	0.708	0.595	0.395	0.394
CarpE	0.381	0.358	0.297	0.337	0.063	0.094
CladF	0.39	0.378	0.187	0.255	0.469	0.482
CrucM	−0.037	−0.112	−1.522	−0.037	−0.062	−0.015
DeadV	0.32	0.322	0.365	0.205	0.340	0.368
ErynM	−0.071	−0.092	−3.54	−0.024	−0.059	−0.023
HeliI	0.699	0.69	0.711	0.668	0.414	0.428
OtanM	−0.094	−0.065	−18.187	−0.045	−0.036	−0.079
SandB	0.977	0.977	0.978	0.889	0.584	0.589
SeseT	0.373	0.469	−0.122	0.422	−0.048	−1.257
ThymC	0.039	0.077	−0.062	0.159	−0.019	−0.042

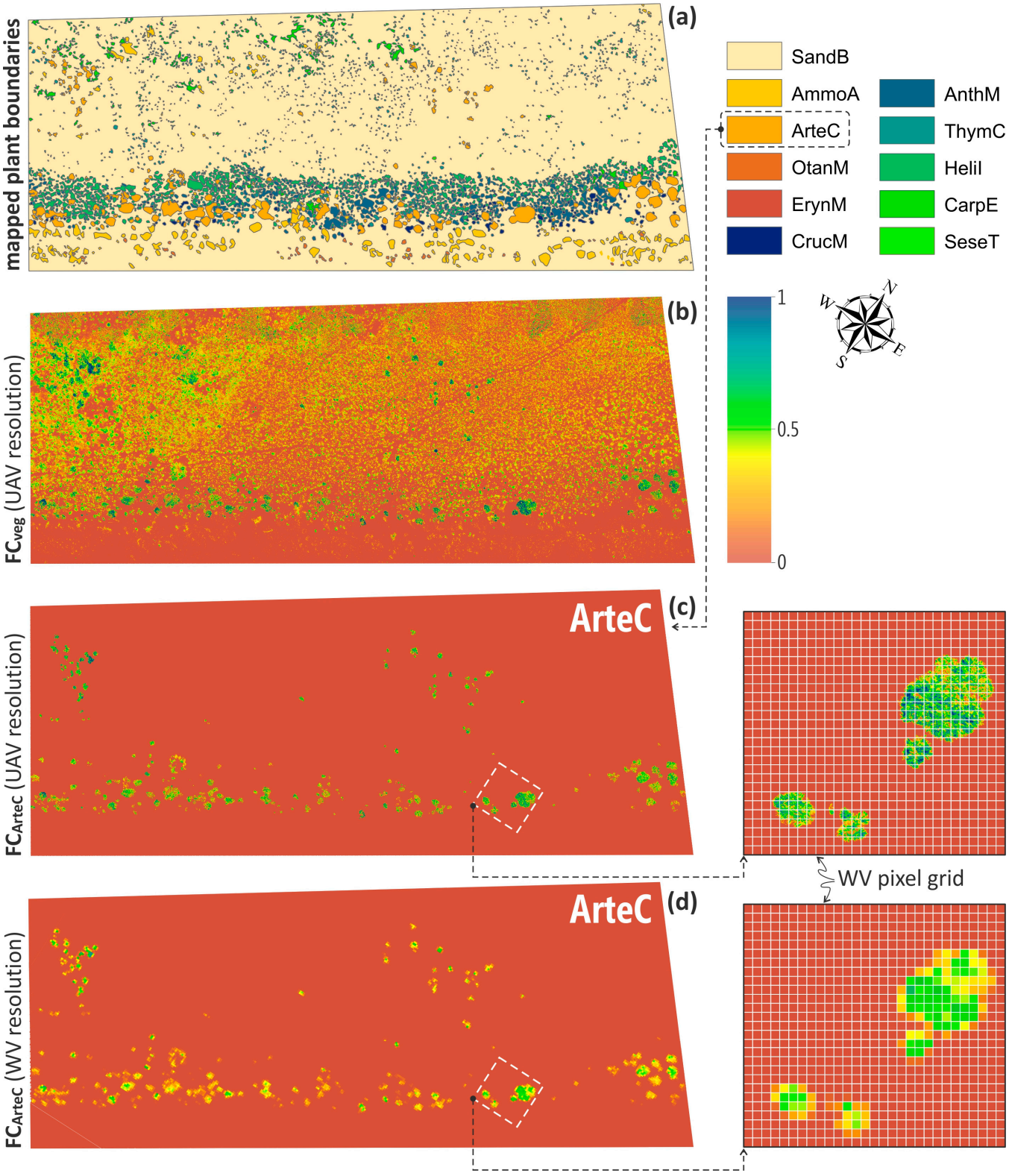

Figure A1. Sequence of data preprocessing steps to obtain the FC of plant species from the UAV data, based on TavW: individual plant boundaries, mapped on high-resolution orthophotos from M2P (**a**), are combined with the FC_{veg} raster ((**b**) obtained from P4M through Equation (1)) to separate the portion of FC_{veg} that corresponds to each dune plant species and then upscale (mean FC_{veg} over the pixel) at the WV pixel size; examples of the FC of ArteC at the original raster resolution and at the WV pixel grid size are given in (**c**) and (**d**), respectively (the zoomed area at the right shows changes in FC after upscaling).

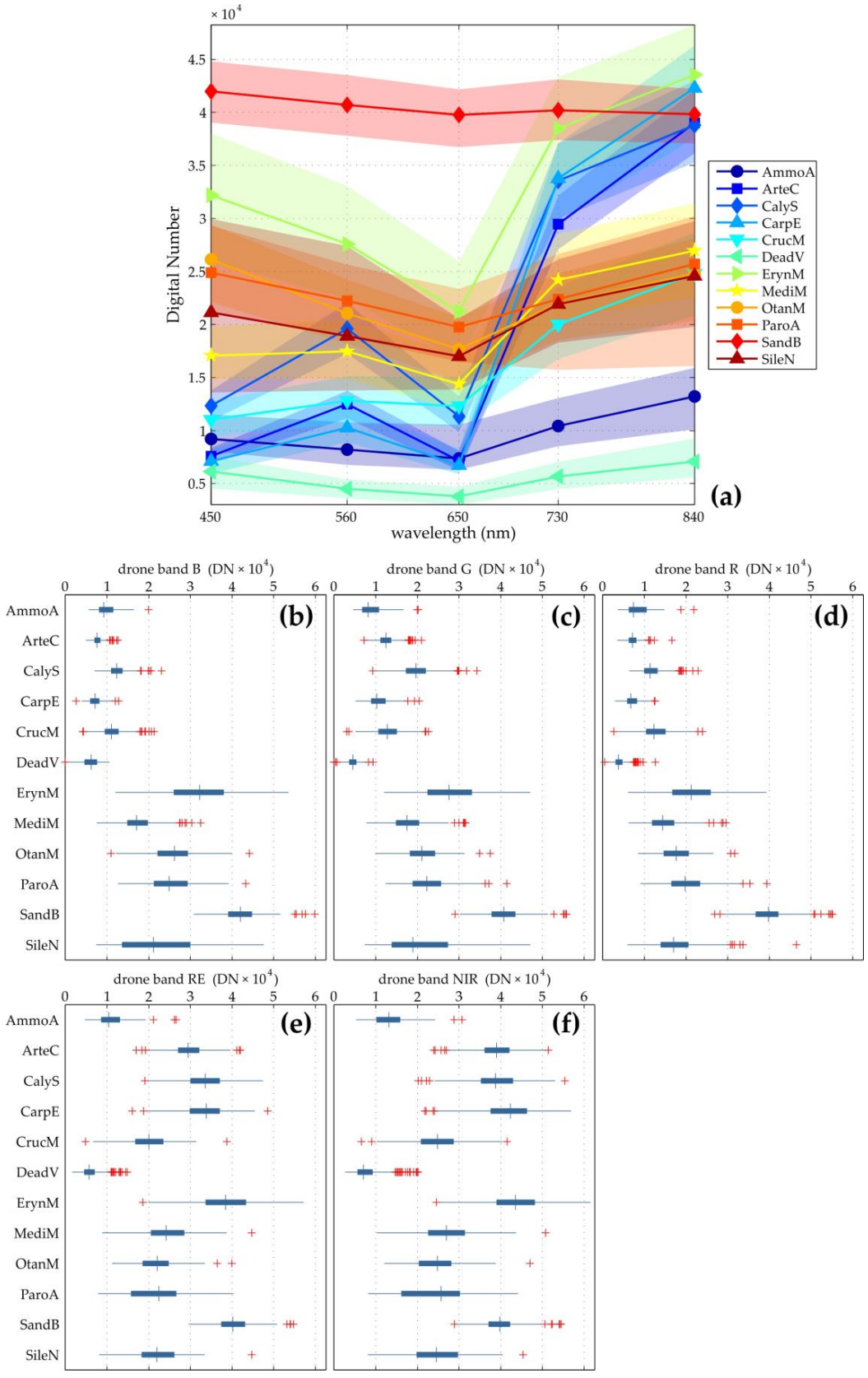

Figure A2. Spectral signature of the main dune plant species and bare sand (SandB) and DeadV classes, obtained from the P4M UAV for AncE, shown as median values (lines) and the range between the 25th and 75th percentiles (shaded area) for all bands (**a**) and boxplots for the blue (**b**), green (**c**), red (**d**), red edge (**e**), and NIR (**f**) bands.

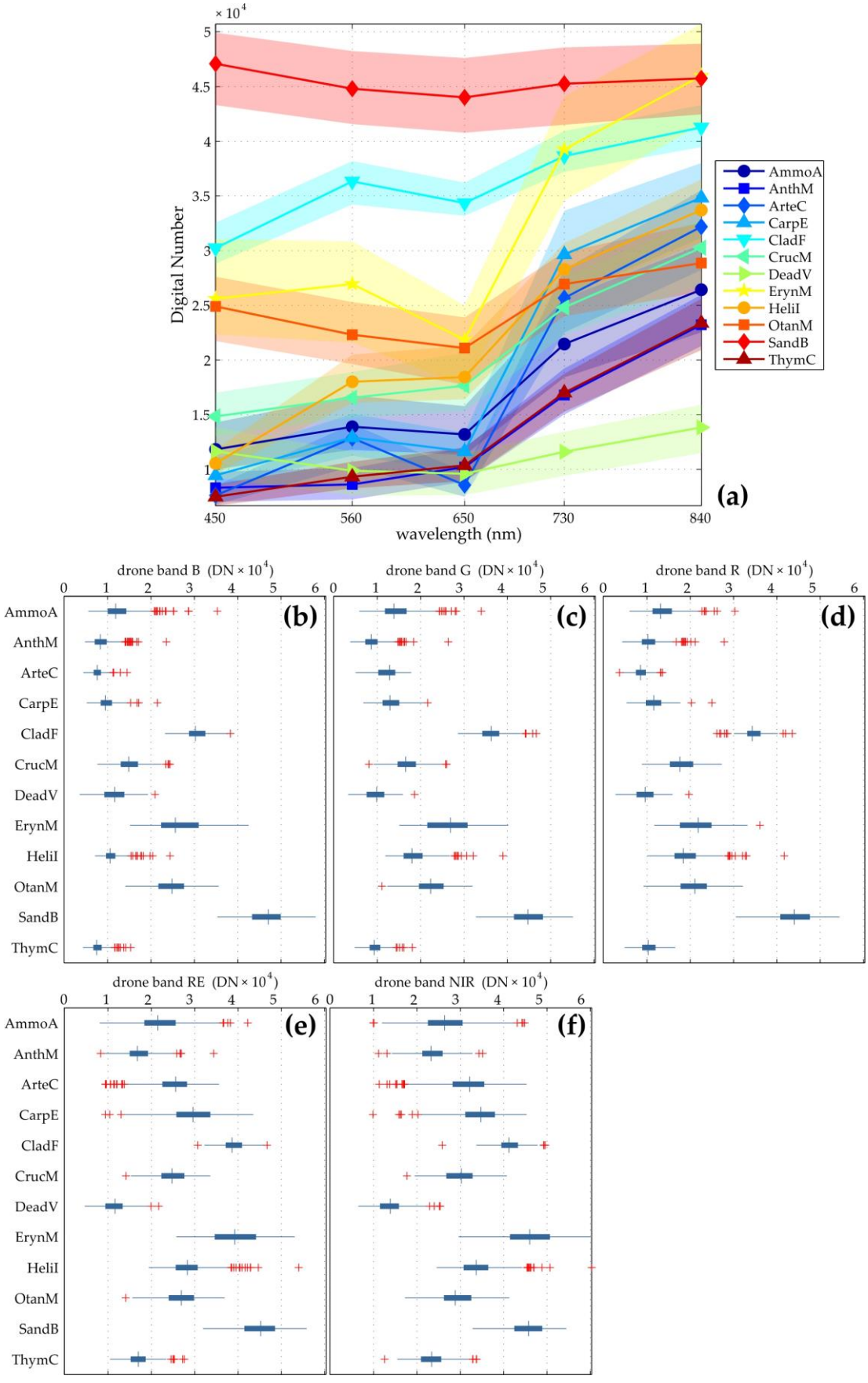

Figure A3. Spectral signature of the main dune plant species and bare sand (SandB) and DeadV classes, obtained from the P4M UAV for TavW, shown as median values (lines) and the range between the 25th and 75th percentiles (shaded area) for all bands (**a**) and boxplots for the blue (**b**), green (**c**), red (**d**), red edge (**e**), and NIR (**f**) bands.

Appendix A.2. RFR Sensitivity and Parameter Tuning

There are several hyperparameters that impact the accuracy of RF algorithms. The main parameters that need to be tuned for performance are [52]:

- The number of trees within the forest (NTree); typically, the higher the number of trees, the better the results in terms of performance and the precision of variable importances; however, the improvement obtained by adding trees diminishes as more and more trees are added.
- The number of drawn candidate variables in each split (min_samples_split), which for the case of RFR is proposed to be 1/4.
- The maximum tree depth (max_depth), which represents the longest path from the root node to the leaf node.

The variability of the coefficient of determination (CoD) with the values of parameters NTree and max_depth for different classes is given in Figure A4. It is noted that the model is largely stable for the NTree parameter, with the accuracy remaining practically unchanged in all classes for NTree > 150. The max_depth parameter produces higher variability in model accuracy, showing a high impact on model skill for some of the classes. Most classes show stablilised CoD values for max_depth > 15, while ErynM and SileN obtain stable accuracy scores after max_depth > 20.

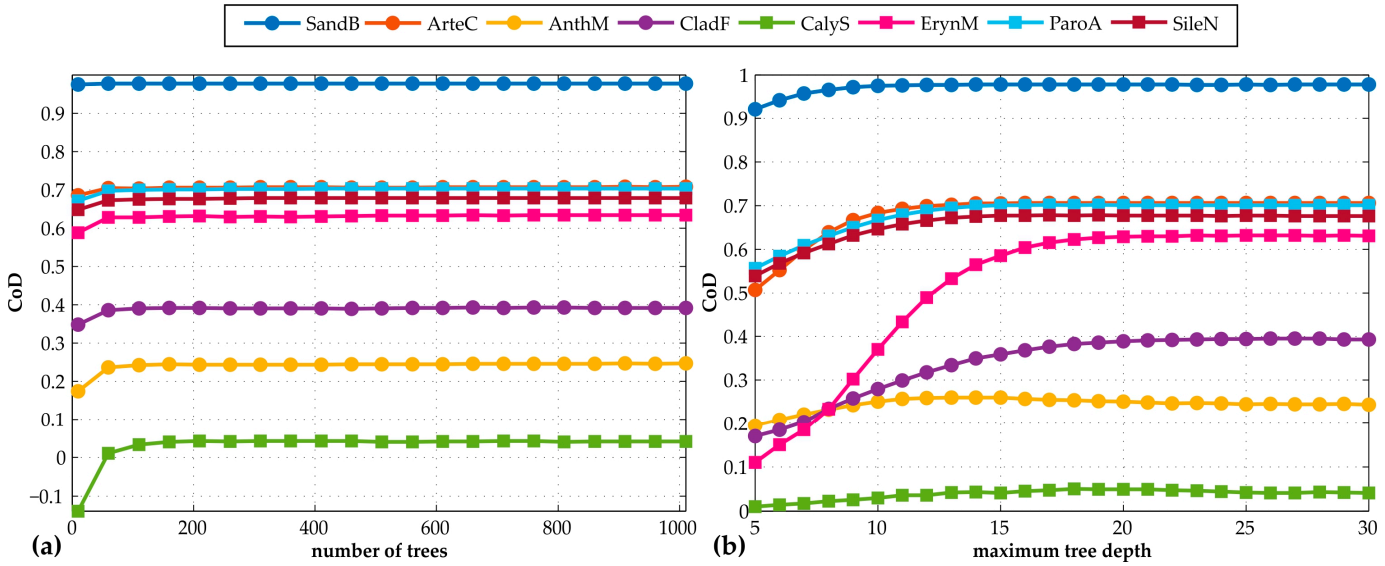

Figure A4. Sensitivity of model skill (CoD) to (**a**) the number of trees and (**b**) the maximum tree depth considered for different classes (circle and square symbols correspond to data from TavW and AncE, respectively).

Based on these results, the main tuning parameters were set at NTree = 500 (maintaining a high number of trees—even though the same skill being achieved by lower values—was considered as the safest choice) and max_depth = 15 (to avoid overfitting).

Appendix A.3. RFR WV2 Predictions Analysed as a Binary Problem

The results of RFR for the WV2 application were used to assess the predictive capacity of the algorithm using tools typically applied in hard classification approaches, such as confusion matrices and related performance metrics. To do this, the predicted (and observed) FC values were translated into presence/absence assuming a floor value of 0.005 for FC. Given that the results of spectral unmixing algorithms allow calculating only the diagonal elements of a typical confusion matrix (i.e., true positives; model mispredictions cannot be attributed to a specific class, as individual RFR forests predict the FC distribution of each

class), individual binary confusion matrices were built for each of the 13 classes in the plots of AncE and TavW (Figure A5).

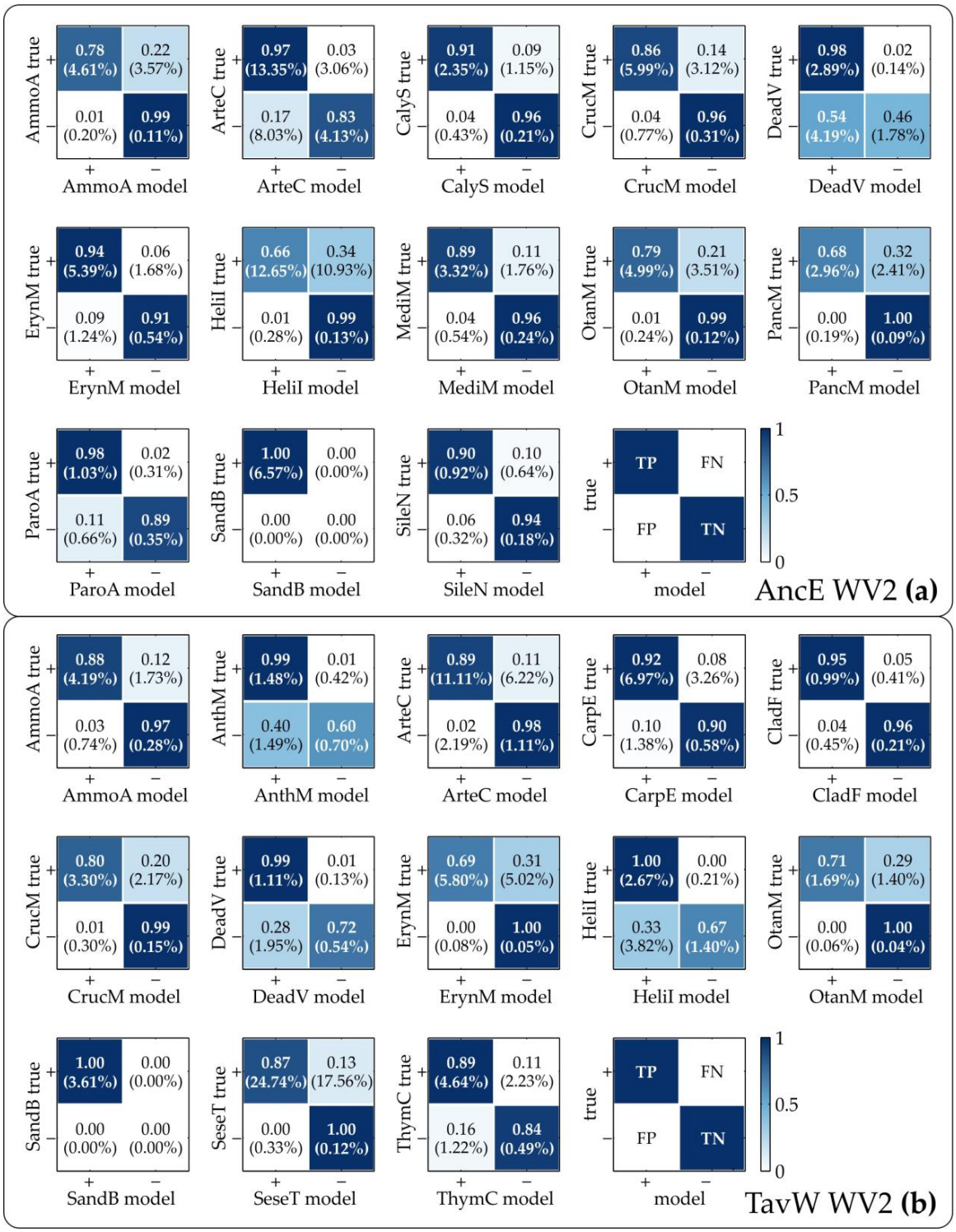

Figure A5. Individual binary normalised confusion matrices for each class from the results of the RFR using WV2 data for AncE (**a**) and TavW (**b**). True positives (TPs), true negatives (TNs), false positives (FPs), and false negatives (FNs) were calculated as the number of pixels where the class was correctly predicted, correctly not predicted, incorrectly predicted, and incorrectly not predicted, respectively, normalised by the total value of pixels in the image (TN equals 0 for class SandB, due to the class being present in all pixels); values in parentheses show RMSEs in %.

Various performance metrics (accuracy, precision, recall, F1 score, and Cohen's kappa), calculated based on these matrices:

$$\text{accuracy} = \frac{\text{TP} + \text{TN}}{\text{TP} + \text{FP} + \text{TN} + \text{FN}} \tag{A1}$$

$$\text{precision} = \frac{\text{TP}}{\text{TP} + \text{FP}} \tag{A2}$$

$$\text{recall} = \frac{\text{TP}}{\text{TP} + \text{FN}} \tag{A3}$$

$$\text{F1 score} = \frac{2 \times \text{precision} \times \text{recall}}{\text{precision} + \text{recall}} \tag{A4}$$

$$\text{recall} = \frac{2 \times (\text{TP} \times \text{TN} - \text{FN} \times \text{FP})}{(\text{TP} + \text{FP}) \times (\text{FP} + \text{TN}) + (\text{TP} + \text{FN}) \times (\text{FN} + \text{TN})} \tag{A5}$$

where TP, TN, FP, and FN are true positives, true negatives, false positives, and false negatives, respectively. The indicator values are given in Figure A6 and show high accuracy and recall for most classes in both plots, and mostly lower precision values. This shows that while the model is indeed effective overall at detecting true instances (low false negatives), it may misclassify species, showing high false positives in some of the classes (e.g., AmmoA, CarpE, CrucM, SeseT, and ThymC). AnthM achieved an F1 score of around 0.8 (Figure A6), indicating the overall balanced performance of the algorithm for the class, despite the very poor CoD (Figure 8a).

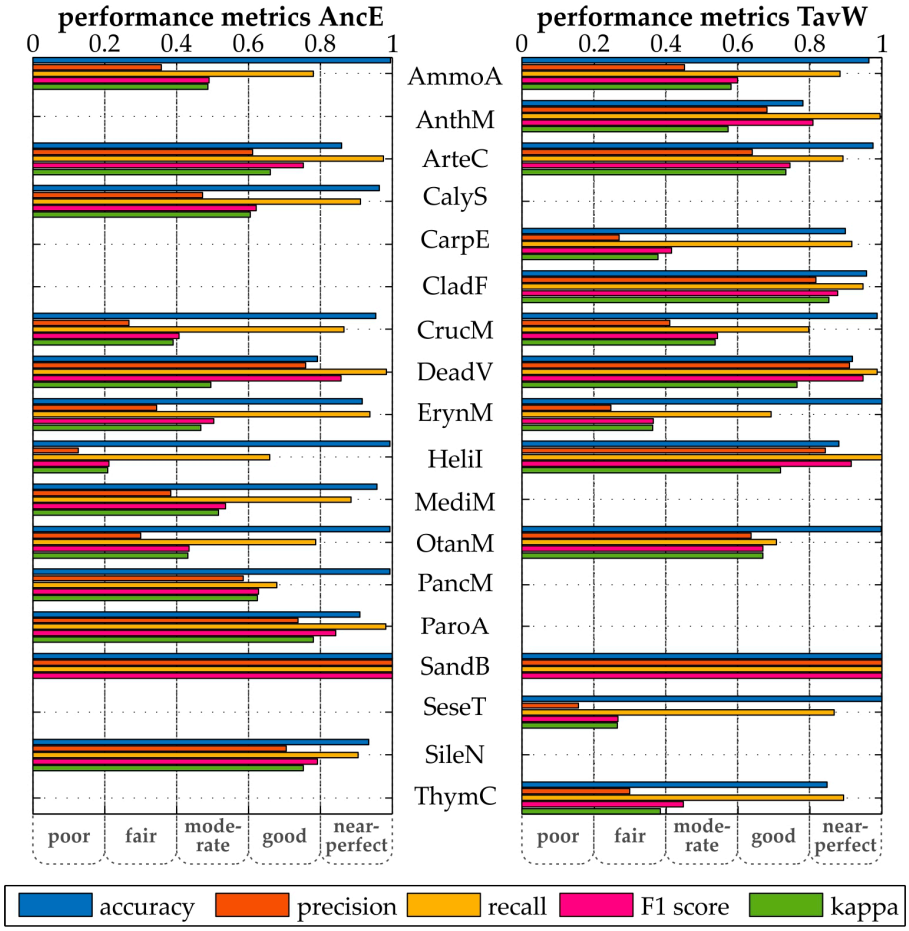

Figure A6. Performance indicators for the RFR application using WV2 data, determined from individual binary confusion matrices for each class (see Figure A5): accuracy, precision, recall, F1 score, and Cohen's kappa, calculated through Equations (A1)–(A5).

Appendix A.4. RFR Using PlanetScope Imagery

Multispectral imagery from the PlanetScope (PS) satellite (Level 3B, Ortho Analytic, eight bands, surface reflectance; spatial resolution of 3 m; acquisition 19 July 2024) were also tested at the TavW plot, following the post-processing analysis described in Section 2.2 and Figure 2, adapted at the spatial resolution of PS.

The RFR performance using WV and PS surface reflectance in each of the classes is shown in Figure A7, where it can be noted that RFR with PS appears to outperform RFR with WV for some classes like CrucM, OtanM, AnthM, HeliI, and DeadV. Interestingly, it also significantly underperforms for the class of ArteC, which is the plant species that showed the highest skill in WV. The difference between the observed and predicted FC (absolute error) for AnthM, ArteC, CladF, CrucM, DeadV, and HeliI is given in Figure A8. These error maps show that RFR with PS data appears more skilful in reproducing the location and FCs of small-scale plants, like OtanM and CrucM that RFR with WV, whereas the error for the bushy ArteC, or more abundant classes like DeadV, is rather high. It needs to be noted that the change in spatial scale (0.5 m for WV to 3 m for PS) means that the pixel grid of PS is 36 times larger, and therefore the FCs are significantly reduced (e.g., the maximum FC for ArteC in TavW is 0.307 for PS and 0.82 for WV, whereas for CrucM the corresponding values are 0.04 and 0.33). It therefore is likely that the better model performance with PS for low FC classes is more related to error diffusion than higher actual skill.

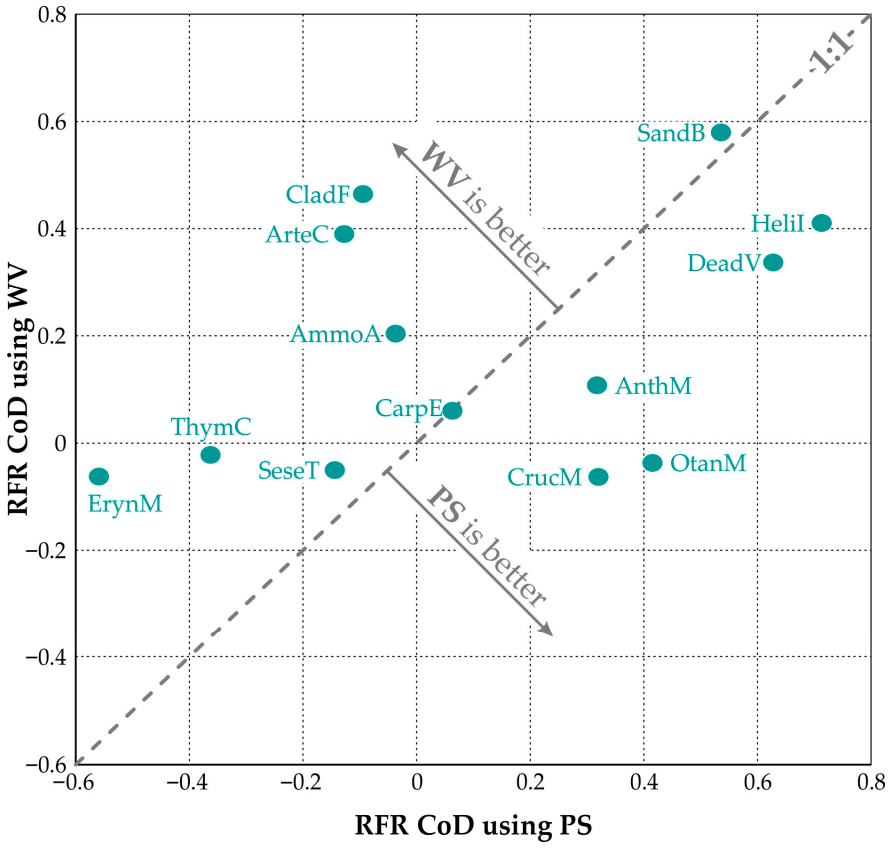

Figure A7. RFR model accuracy (CoD) using WV (y axes) versus PS (x axis) imagery; results are from TavW.

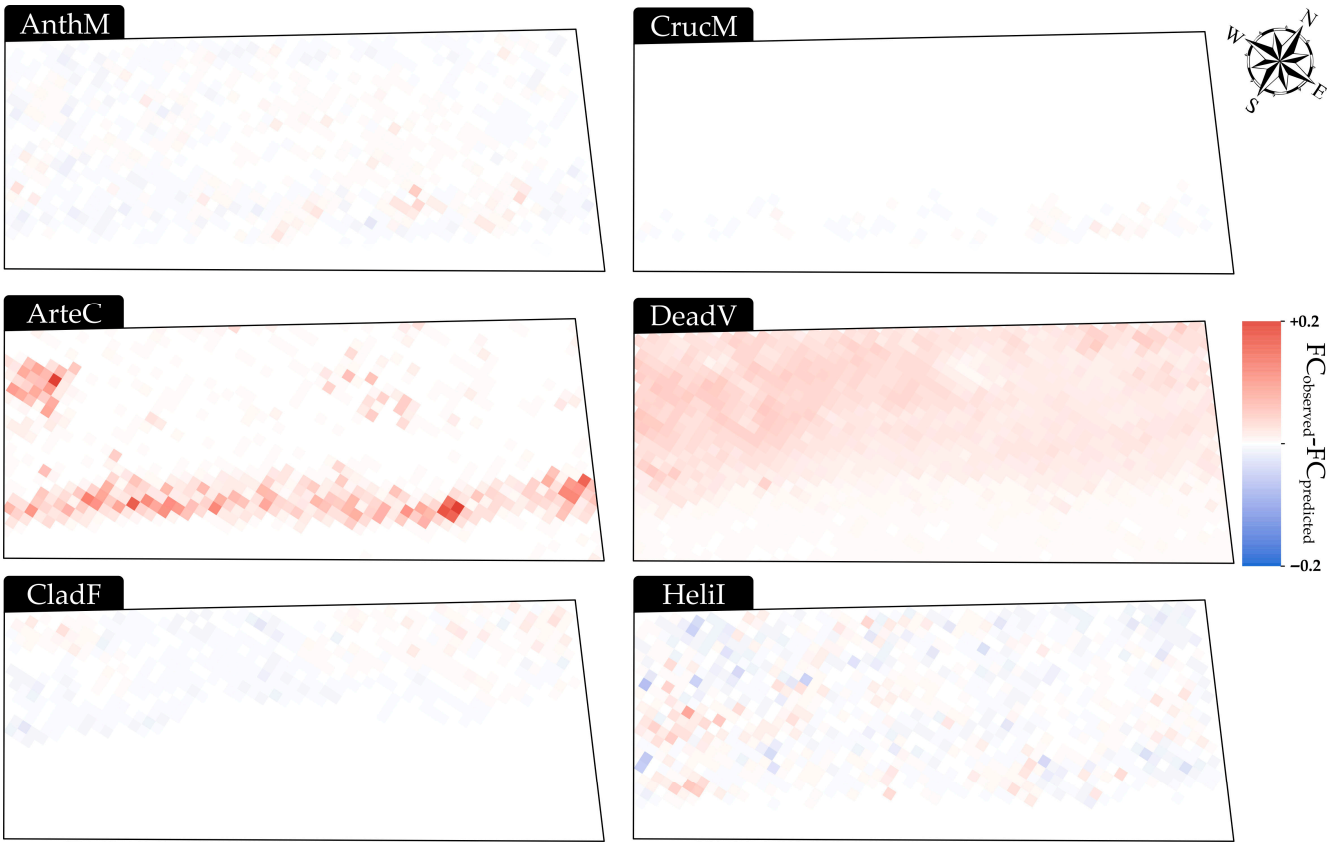

Figure A8. Absolute error (observed–predicted) in FC of indicative classes in TavW using RFR with PS radiometric data.

References

1. Sperandii, M.G.; Barták, V.; Carboni, M.; Acosta, A.T.R. Getting the Measure of the Biodiversity Crisis in Mediterranean Coastal Habitats. *J. Ecol.* **2021**, *109*, 1224–1235. [CrossRef]
2. Costas, S.; de Sousa, L.B.; Kombiadou, K.; Ferreira, Ó.; Plomaritis, T.A. Exploring Foredune Growth Capacity in a Coarse Sandy Beach. *Geomorphology* **2020**, *371*, 107435. [CrossRef]
3. Gallego-Fernández, J.B.; Muñoz-Valles, S.; Dellafiore, C.M. Spatio-Temporal Patterns of Colonization and Expansion of Retama Monosperma on Developing Coastal Dunes. *J. Coast. Conserv.* **2015**, *19*, 577–587. [CrossRef]
4. Gallego-Fernández, J.B.; Martínez, M.L.; García-Franco, J.G.; Zunzunegui, M. The Impact on Plant Communities of an Invasive Alien Herb, Oenothera Drummondii, Varies along the Beach-Coastal Dune Gradient. *Flora* **2019**, *260*, 151466. [CrossRef]
5. Kang, L.; Zhang, M.; Li, C.; Yang, Z. Effect of Plant Shapes on Sand Transport Rate and Aerodynamic Particle Entrainment Rate from the Perspective of Plant Drag. *Catena* **2024**, *237*, 107818. [CrossRef]
6. Kombiadou, K.; Matias, A.; Costas, S.; Rita Carrasco, A.; Plomaritis, T.A.; Ferreira, Ó. Barrier Island Resilience Assessment: Applying the Ecological Principles to Geomorphological Data. *Catena* **2020**, *194*, 104755. [CrossRef]
7. Medina Machín, A.; Marcello, J.; Hernández-Cordero, A.I.; Martín Abasolo, J.; Eugenio, F. Vegetation Species Mapping in a Coastal-Dune Ecosystem Using High Resolution Satellite Imagery. *GIsci. Remote Sens.* **2019**, *56*, 210–232. [CrossRef]
8. Jackson, D.W.T.; Costas, S.; González-Villanueva, R.; Cooper, A. A Global 'Greening' of Coastal Dunes: An Integrated Consequence of Climate Change? *Glob. Planet. Change* **2019**, *182*, 103026. [CrossRef]
9. Suo, C.; McGovern, E.; Gilmer, A. Coastal Dune Vegetation Mapping Using a Multispectral Sensor Mounted on an UAS. *Remote Sens.* **2019**, *11*, 1814. [CrossRef]
10. Duffy, J.P.; Shutler, J.D.; Witt, M.J.; DeBell, L.; Anderson, K. Tracking Fine-Scale Structural Changes in Coastal Dune Morphology Using Kite Aerial Photography and Uncertainty-Assessed Structure-from-Motion Photogrammetry. *Remote Sens.* **2018**, *10*, 1494. [CrossRef]
11. Xue, J.; Su, B. Significant Remote Sensing Vegetation Indices: A Review of Developments and Applications. *J. Sens.* **2017**, *2017*, 1353691. [CrossRef]
12. Cruz, C.; O'Connell, J.; McGuinness, K.; Martin, J.R.; Perrin, P.M.; Connolly, J. Assessing the Effectiveness of UAV Data for Accurate Coastal Dune Habitat Mapping. *Eur. J. Remote Sens.* **2023**, *56*, 2191870. [CrossRef]

13. Innangi, M.; Di Febbraro, M.; Balsi, M.; Colonna, G.; Finizio, M.; Pontieri, F.; Carranza, M.L. A Novel High-Resolution Eco-Functional Vegetation Mapping of Coastal Dunes. *Ecol. Indic.* **2025**, *171*, 113157. [CrossRef]
14. Laporte-Fauret, Q.; Castelle, B.; Marieu, V.; Bujan, S.; Michalet, R.; Rosebery, D. Coastal Dune Morphology Evolution Combining Lidar and UAV Surveys, Truc Vert Beach 2011–2019. *J. Coast. Res.* **2020**, *95*, 163–167. [CrossRef]
15. De Giglio, M.; Greggio, N.; Goffo, F.; Merloni, N.; Dubbini, M.; Barbarella, M. Comparison of Pixel- and Object-Based Classification Methods of Unmanned Aerial Vehicle Data Applied to Coastal Dune Vegetation Communities: Casal Borsetti Case Study. *Remote Sens.* **2019**, *11*, 1416. [CrossRef]
16. Demichele, D.; Belcore, E.; Piras, M.; Camporeale, C. Species-By-Species Pattern Analysis of Coastal Dune Vegetation. *J. Geophys. Res. Biogeosci* **2025**, *130*, e2024JG008419. [CrossRef]
17. Belcore, E.; Latella, M.; Piras, M.; Camporeale, C. Enhancing Precision in Coastal Dunes Vegetation Mapping: Ultra-High Resolution Hierarchical Classification at the Individual Plant Level. *Int. J. Remote Sens.* **2024**, *45*, 4527–4552. [CrossRef]
18. Meyer, M.D.F.; Gonçalves, J.A.; Cunha, J.F.R.; Ramos, S.C.D.C.E.S.; Bio, A.M.F. Application of a Multispectral UAS to Assess the Cover and Biomass of the Invasive Dune Species Carpobrotus Edulis. *Remote Sens.* **2023**, *15*, 2411. [CrossRef]
19. Lansu, E.M.; Reijers, V.C.; Daniëls, F.; James, R.; Christianen, M.J.A.; van der Heide, T. Habitat Mapping of Coastal Dunes with Deep Learning. *Ecol. Inform.* **2025**, *92*, 103444. [CrossRef]
20. McAllister, E.; Payo, A.; Novellino, A.; Dolphin, T.; Medina-Lopez, E. Multispectral Satellite Imagery and Machine Learning for the Extraction of Shoreline Indicators. *Coast. Eng.* **2022**, *174*, 104102. [CrossRef]
21. Yousefi Lalimi, F.; Silvestri, S.; Moore, L.J.; Marani, M. Coupled Topographic and Vegetation Patterns in Coastal Dunes: Remote Sensing Observations and Ecomorphodynamic Implications. *J. Geophys. Res. Biogeosci* **2017**, *122*, 119–130. [CrossRef]
22. Garzon, J.L.; Costas, S.; Ferreira, O. Biotic and Abiotic Factors Governing Dune Response to Storm Events. *Earth Surf. Process. Landf.* **2021**, *47*, 1013–1031. [CrossRef]
23. Kozhoridze, G.; Ben Dor, E.; Sternberg, M. Assessing the Dynamics of Plant Species Invasion in Eastern-Mediterranean Coastal Dunes Using Cellular Automata Modeling and Satellite Time-Series Analyses. *Remote Sens.* **2022**, *14*, 1014. [CrossRef]
24. Marzialetti, F.; Giulio, S.; Malavasi, M.; Sperandii, M.G.; Acosta, A.T.R.; Carranza, M.L. Capturing Coastal Dune Natural Vegetation Types Using a Phenology-Based Mapping Approach: The Potential of Sentinel-2. *Remote Sens.* **2019**, *11*, 1506. [CrossRef]
25. Marzialetti, F.; Di Febbraro, M.; Malavasi, M.; Giulio, S.; Rosario Acosta, A.T.; Carranza, M.L. Mapping Coastal Dune Landscape through Spectral Rao's Q Temporal Diversity. *Remote Sens.* **2020**, *12*, 2315. [CrossRef]
26. Gupta, S.K.; Ben-Dor, E.; Sternberg, M. Unveiling the Invasion: Advancing Ecological Mapping of Heterotheca Subaxillaris Through Integrated Remote Sensing Techniques with Drones and Satellites. *IEEE J. Sel. Top. Appl. Earth Obs. Remote Sens.* **2024**, *17*, 7193–7211. [CrossRef]
27. Marzialetti, F.; Di Febbraro, M.; Frate, L.; De Simone, W.; Acosta, A.T.R.; Carranza, M.L. Synergetic Use of Unmanned Aerial Vehicle and Satellite Images for Detecting Non-Native Tree Species: An Insight into Acacia Saligna Invasion in the Mediterranean Coast. *Front. Environ. Sci.* **2022**, *10*, 880626. [CrossRef]
28. Yang, Z.; D'alpaos, A.; Marani, M.; Silvestri, S. Assessing the Fractional Abundance of Highly Mixed Salt-Marsh Vegetation Using Random Forest Soft Classification. *Remote Sens.* **2020**, *12*, 3224. [CrossRef]
29. Yang, Z.; Blount, T.; Lester, C.; Blackford, N.; D'Alpaos, A.; Marani, M.; Murray, B.; Silvestri, S. Unmixing Marsh Vegetation Species across Multiple Sensors and Spatial Scales. *GIsci. Remote Sens.* **2025**, *62*, 2481689. [CrossRef]
30. Cavalli, R.M. Spatial Validation of Spectral Unmixing Results: A Case Study of Venice City. *Remote Sens.* **2022**, *14*, 5165. [CrossRef]
31. Ettritch, G.; Bunting, P.; Jones, G.; Hardy, A. Monitoring the Coastal Zone Using Earth Observation: Application of Linear Spectral Unmixing to Coastal Dune Systems in Wales. *Remote Sens. Ecol. Conserv.* **2018**, *4*, 303–319. [CrossRef]
32. Pafumi, E.; Angiolini, C.; Bacaro, G.; Fanfarillo, E.; Fiaschi, T.; Rocchini, D.; Sarmati, S.; Torresani, M.; Feilhauer, H.; Maccherini, S. Fuzzy Approaches Provide Improved Spatial Detection of Coastal Dune EU Habitats. *Ecol. Inform.* **2025**, *86*, 103059. [CrossRef]
33. Costas, S.; Gallego-Fernández, J.B.; Bon de Sousa, L.; Kombiadou, K. Ecogeomorphic Response of a Coastal Dune in Southern Portugal Regulated by Extrinsic Factors. *Catena* **2023**, *221*, 106796. [CrossRef]
34. Mora, C.; Vieira, G. The Climate of Portugal. In *World Geomorphological Landscapes*; Springer: Cham, Switzerland, 2020; pp. 33–46. [CrossRef]
35. IPMA, Instituto Português Do Mar e Da Atmosfera. Available online: https://www.ipma.pt/en/index.html (accessed on 2 July 2025).
36. Maurer, T. How to Pansharpen Images Using the Gram-Schmidt Pan-Sharpen Method—A Recipe. *Int. Arch. Photogramm. Remote Sens. Spat. Inf. Sci.* **2013**, *XL-1/W1*, 239–244. [CrossRef]
37. Gram-Schmidt Pan Sharpening. Available online: https://www.nv5geospatialsoftware.com/docs/GramSchmidtSpectralSharpening.html (accessed on 14 January 2025).
38. Bon de Sousa, L.B.; Costas, S.; Ferreira, Ó. Effect of Survey Parameters on Unmanned Aerial Vehicles-Derived Topography for Coastal Dune Monitoring. *J. Appl. Remote Sens.* **2022**, *16*, 34513. [CrossRef]

39. Breiman, L. Random Forests. *Mach. Learn.* **2001**, *45*, 5–32. [CrossRef]
40. Genuer, R. Variance Reduction in Purely Random Forests. *J. Nonparametric Stat.* **2012**, *24*, 543–562. [CrossRef]
41. RandomForestRegressor—Scikit-Learn 1.6.1 Documentation. Available online: https://scikit-learn.org/stable/modules/generated/sklearn.ensemble.RandomForestRegressor.html (accessed on 10 January 2025).
42. Gao, L.; Wang, X.; Johnson, B.A.; Tian, Q.; Wang, Y.; Verrelst, J.; Mu, X.; Gu, X. Remote Sensing Algorithms for Estimation of Fractional Vegetation Cover Using Pure Vegetation Index Values: A Review. *ISPRS J. Photogramm. Remote Sens.* **2020**, *159*, 364–377. [CrossRef]
43. Liu, Q.; Zhang, T.; Li, Y.; Li, Y.; Bu, C.; Zhang, Q. Comparative Analysis of Fractional Vegetation Cover Estimation Based on Multi-Sensor Data in a Semi-Arid Sandy Area. *Chin. Geogr. Sci.* **2018**, *29*, 166–180. [CrossRef]
44. Choi, S.K.; Lee, S.K.; Jung, S.H.; Choi, J.W.; Choi, D.Y.; Chun, S.J. Estimation of Fractional Vegetation Cover in Sand Dunes Using Multi-Spectral Images from Fixed-Wing UAV. *J. Korean Soc. Surv. Geod. Photogramm. Cartogr.* **2016**, *34*, 431–441. [CrossRef]
45. Zhang, X.; Liao, C.; Li, J.; Sun, Q. Fractional Vegetation Cover Estimation in Arid and Semi-Arid Environments Using HJ-1 Satellite Hyperspectral Data. *Int. J. Appl. Earth Obs. Geoinf.* **2013**, *21*, 506–512. [CrossRef]
46. Han, J.; Zhu, J.; Cao, X.; Xi, L.; Qi, Z.; Li, Y.; Wang, X.; Zou, J. Extraction of Sparse Vegetation Cover in Deserts Based on UAV Remote Sensing. *Remote Sens.* **2025**, *17*, 2665. [CrossRef]
47. Gutman, G.; Ignatov, A. The Derivation of the Green Vegetation Fraction from NOAA/AVHRR Data for Use in Numerical Weather Prediction Models. *Int. J. Remote Sens.* **1998**, *19*, 1533–1543. [CrossRef]
48. Macedo, F.L.; Nóbrega, H.; de Freitas, J.G.R.; Pinheiro de Carvalho, M.A.A. Assessment of Vegetation Indices Derived from UAV Imagery for Weed Detection in Vineyards. *Remote Sens.* **2025**, *17*, 1899. [CrossRef]
49. Smyth, T.A.G.; Wilson, R.; Rooney, P.; Yates, K.L. Extent, Accuracy and Repeatability of Bare Sand and Vegetation Cover in Dunes Mapped from Aerial Imagery Is Highly Variable. *Aeolian Res.* **2022**, *56*, 100799. [CrossRef]
50. Probst, P.; Wright, M.N.; Boulesteix, A.L. Hyperparameters and Tuning Strategies for Random Forest. *Wiley Interdiscip. Rev. Data Min. Knowl. Discov.* **2019**, *9*, e1301. [CrossRef]
51. Légaré, B.; Bélanger, S.; Singh, R.K.; Bernatchez, P.; Cusson, M. Remote Sensing of Coastal Vegetation Phenology in a Cold Temperate Intertidal System: Implications for Classification of Coastal Habitats. *Remote Sens.* **2022**, *14*, 3000. [CrossRef]
52. Dennison, P.E.; Halligan, K.Q.; Roberts, D.A. A Comparison of Error Metrics and Constraints for Multiple Endmember Spectral Mixture Analysis and Spectral Angle Mapper. *Remote Sens. Environ.* **2004**, *93*, 359–367. [CrossRef]
53. Cohen, J. A Coefficient of Agreement for Nominal Scales. *Educ. Psychol. Meas.* **1960**, *20*, 37–46. [CrossRef]
54. Nikoo, M.R.; Zamani, M.G.; Zadeh, M.M.; Al-Rawas, G.; Al-Wardy, M.; Gandomi, A.H. Mapping Reservoir Water Quality from Sentinel-2 Satellite Data Based on a New Approach of Weighted Averaging: Application of Bayesian Maximum Entropy. *Sci. Rep.* **2024**, *14*, 16438. [CrossRef]
55. Krawczyk, B. Learning from Imbalanced Data: Open Challenges and Future Directions. *Prog. Artif. Intell.* **2016**, *5*, 221–232. [CrossRef]
56. Torgo, L.; Branco, P.; Ribeiro, R.P.; Pfahringer, B. Resampling Strategies for Regression. *Expert Syst.* **2015**, *32*, 465–476. [CrossRef]
57. Franklin, B.; Moore, L.J.; Zinnert, J.C. Predicting Barrier Island Shrub Presence Using Remote Sensing Products and Machine Learning Techniques. *J. Geophys. Res. Earth Surf.* **2024**, *129*, e2023JF007465. [CrossRef]
58. Burvingt, O.; Castelle, B.; Marieu, V.; Lubac, B.; Nicolae Lerma, A.; Robin, N. Using Pleiades Satellite Imagery to Monitor Multi-Annual Coastal Dune Morphological Changes. *Remote Sens.* **2025**, *17*, 1522. [CrossRef]
59. Costas, S.; Bon de Sousa, L.; Gallego-Fernández, J.B.; Hesp, P.; Kombiadou, K. Foredune Initiation and Early Development through Biophysical Interactions. *Sci. Total Environ.* **2024**, *940*, 173548. [CrossRef]
60. Cini, E.; Marzialetti, F.; Paterni, M.; Berton, A.; Acosta, A.T.R.; Ciccarelli, D. Integrating UAV Imagery and Machine Learning via Geographic Object Based Image Analysis (GEOBIA) for Enhanced Monitoring of Yucca Gloriosa in Mediterranean Coastal Dunes. *Ocean Coast. Manag.* **2024**, *258*, 107377. [CrossRef]
61. Kombiadou, K.; Costas, S.; Roelvink, D. Exploring Controls on Coastal Dune Growth Through a Simplified Model. *J. Geophys. Res. Earth Surf.* **2023**, *128*, e2023JF007080. [CrossRef]
62. van Kuik, N.; de Vries, J.; Schwarz, C.; Ruessink, G. Surface-Area Development of Foredune Trough Blowouts and Associated Parabolic Dunes Quantified from Time Series of Satellite Imagery. *Aeolian Res.* **2022**, *57*, 100812. [CrossRef]
63. Talavera, L.; Costas, S.; Ferreira, Ó. A New Index to Assess the State of Dune Vegetation Derived from True Colour Images. *Ecol. Indic.* **2022**, *137*, 108770. [CrossRef]